Award Number 06HQGR0105

# SYSTEMATIC TEMPORAL AND SPATIAL SEISMIC ANISOTROPY STUDY AROUND PARKFIELD, CALIFORNIA

Haijiang Zhang, Yunfeng Liu, and Clifford Thurber

Department of Geology and Geophysics
University of Wisconsin-Madison
1215 W. Dayton Street
Madison WI 53706, U.S.A.

Tel: 608-262-1921
Fax: 608-262-0693

E-mails: hjzhang@geology.wisc.edu (HZ)
yunfengl@geology.wisc.edu (YL)
thurber@geology.wisc.edu (CH)

March 26, 2007

Award Number 06HQGR0105

# SYSTEMATIC TEMPORAL AND SPATIAL SEISMIC ANISOTROPY STUDY AROUND PARKFIELD, CALIFORNIA

Haijiang Zhang, Yunfeng Liu, and Clifford Thurber

Department of Geology and Geophysics, University of Wisconsin-Madison
1215 W. Dayton Street, Madison, WI 53706

Tel: (608) 262-1921; Fax: (608) 262-0693;
E-mail: hjzhang@geology.wisc.edu; yunfengl@geology.wisc.edu; thurber@geology.wisc.edu

**Abstract**

We systematically analyzed shear wave splitting for seismic data observed at a temporary array and two permanent networks around the San Andreas Fault Observatory at Depth. The purpose was to investigate the spatial distribution of crustal shear wave anisotropy around the San Andreas Fault in this segment and its temporal behavior in relation to the occurrence of the 2004 Parkfield M 6.0 earthquake. The dense coverage of the networks, the accurate locations of earthquakes and the high-resolution velocity model provide a unique opportunity to investigate anisotropy in detail around the San Andreas Fault zone. The results show that the primary fast polarization directions in the region including the San Andreas Fault zone and the northeast side of the fault are NW-SE, nearly parallel or subparallel to the San Andreas Fault strike. Some measurements on the southwest side of the fault are oriented to the NNE-SSW direction, approximately parallel to the direction of local maximum horizontal compressive stress. There are also a few areas in which the observed fast PDs do not fit into this general pattern.

The strong spatial variations in both the measured fast polarization directions and time delays reveal the extreme complexity of shear wave anisotropy in the area. The top 2-3 km of the crust appears to contribute the most the observed time delays; however substantial anisotropy could extend to as deep as 7-8 km in the region. To characterize in detail the three-dimensional shear-wave anisotropy structure, we developed an anisotropy tomography method based on the assumption that the measured shear-wave splitting delay times are accumulated along the ray paths. The strength of the anisotropy is indicated by a parameter of anisotropy percentage K. The results indicate that the earthquakes are located in a highly anisotropic fault zone, down to a depth of 4 km. At greater depths, the earthquakes are located in less anisotropic zones. To the southwest of the San Andreas Fault, the Salinian granitic block shows relatively strong anisotropic anomalies that are caused by the aligned microcracks consistent to the direction of the maximum compressive horizontal stress. To the northeast of the fault zone, a strong anisotropic anomaly corresponds to the serpentinite body sandwiched between Franciscan rocks.

We also analyzed temporal patterns of shear wave splitting parameters in a nearly 4 year period around the 2004 Parkfield mainshock based on similar events. The results show that there are no appreciable precursory, co-seismic, or post-seismic temporal changes of shear wave splitting in a region near the rupture of an M 6.0 earthquake, about 15 km away from its epicenter.

## 1 INTRODUCTION

Shear wave splitting (SWS) in the crust surrounding active fault zones has been studied extensively (e.g. Zhang & Schwartz 1994; Bouin *et al.* 1996; Peng & Ben-Zion 2004; Mizuno *et al.* 2005), including numerous efforts targeted on the segment of the San Andreas Fault (SAF) near Parkfield, California (Liu *et al.* 1997; Boness & Zoback 2004, 2006; Cochran *et al.* 2006). Liu *et al.* (1997) analyzed recordings at UC-Berkeley High Resolution Seismic Network (HRSN) stations around the SAF to search for spatial and temporal variations in SWS. Boness & Zoback (2004, 2006) systematically investigated seismic anisotropy in the San Andreas Fault Observatory at Depth (SAFOD) Pilot Hole and Main Hole using dipole sonic and microearthquake data. Cochran *et al.* (2006) analyzed SWS on data from two temporary arrays right on the SAF trace near Parkfield. These studies have provided rich information about the anisotropic properties of rocks within the fault zone and nearby crust in relation to the fault zone structure and local stress fields.

SWS is caused by the anisotropy of the medium through which waves propagate. The mechanisms for anisotropy in the upper crust can be divided into two major categories (Boness & Zoback 2006). The first category is stress-induced anisotropy related to alignment of cracks in response to the in-situ stress field. In two related models, extensive dilatancy anisotropy of microcracks (e.g. Crampin 1987) and the preferential closure of fractures in rock (Boness & Zoback 2004), the fast polarization direction (PD) of the vertically propagating shear wave is parallel to the maximum horizontal compressive stress $\sigma_H$. The second category is structural anisotropy associated with aligned planar features such as fault zone fabrics (e.g. Mueller 1991), sedimentary bedding planes (e.g. Leary *at al.* 1990), and aligned minerals/grains (e.g. Kern & Wenk 1990). In this case, the strike of the structural fabrics will control the fast PD of vertically propagating shear waves. Previous studies of SWS in the Parkfield area found that both mechanisms seem to play roles in observed fast PDs depending on the station location. Due to limitation of station coverage in these studies, the detailed spatial distribution of anisotropy in the area has remained unclear. In this study, we take advantage of the dense coverage of the temporary and permanent networks, a catalog of accurate earthquake locations, and a high-resolution velocity model to study systematically the spatial distribution of anisotropy in the SAF zone and its vicinity.

SWS has been claimed to be an effective tool for detecting possible temporal variations of crustal anisotropy around active fault zones associated with earthquakes (e.g. Crampin & Chastin 2003). Findings of temporal changes of SWS have been controversial. A number of studies reported temporal changes before (e.g. Crampin *et al.* 1990; Liu *et al.* 1997), or around (e.g. Saiga *et al.* 2003; Piccinini *et al.* 2006) the occurrence of large or moderate earthquakes. Many other studies have not observed appreciable changes of crustal anisotropy near the epicentral areas of moderate to large earthquakes (e.g. Aster *et al.* 1990, 1991; Munson *et al.* 1995; Cochran *et al.* 2003; Liu *et al.* 2004). Peng & Ben-Zion (2004) and Liu *et al.* (2004, 2005a) showed that spatial variations of anisotropy can be erroneously mapped into temporal changes. The most effective way to separate temporal variations from spatial changes is to use similar events that provide almost identical ray paths. In this study we also analyzed shear wave splitting using a number of clusters of similar events to investigate the temporal behavior of crustal anisotropy around the SAF zone in relation to the 2004 M 6.0 Parkfield earthquake.

## 2 DATASET AND GEOLOGIC SETTING

Seismic waveforms analyzed for shear wave splitting were recorded by the stations of a temporary array known as the Parkfield Area Seismic Observatory (PASO) (Thurber *et al.* 2004), the HRSN and the USGS Northern California Seismic Network (NCSN). The PASO array was installed around the SAFOD site beginning in July 2000. The primary motivation for the deployment was to improve the accuracy of the location of microearthquakes along the SAF in the SAFOD drilling target zone and the knowledge of the three-dimensional (3D) velocity structure in the vicinity of the drill site. Initially, there were 15 3-component seismometers from the Program for the Array Seismic Studies of the Continental Lithosphere (PASSCAL) of the Incorporated Research Institutions for Seismology (IRIS) Consortium. In July 2001, 44 additional PASSCAL 3-component stations were deployed within the aperture of the original array, and two of the original stations were moved. All stations were removed in October 2002. The dataset in this study mainly consists of 575 local earthquakes that occurred from June 2001 to October 2002. The locations of these events and stations are shown in Fig. 1. Additional seismic data from 2000 to 2005, covering the 2004 M6.0 Parkfield earthquake, are also used for studying the temporal variations of SWS parameters.

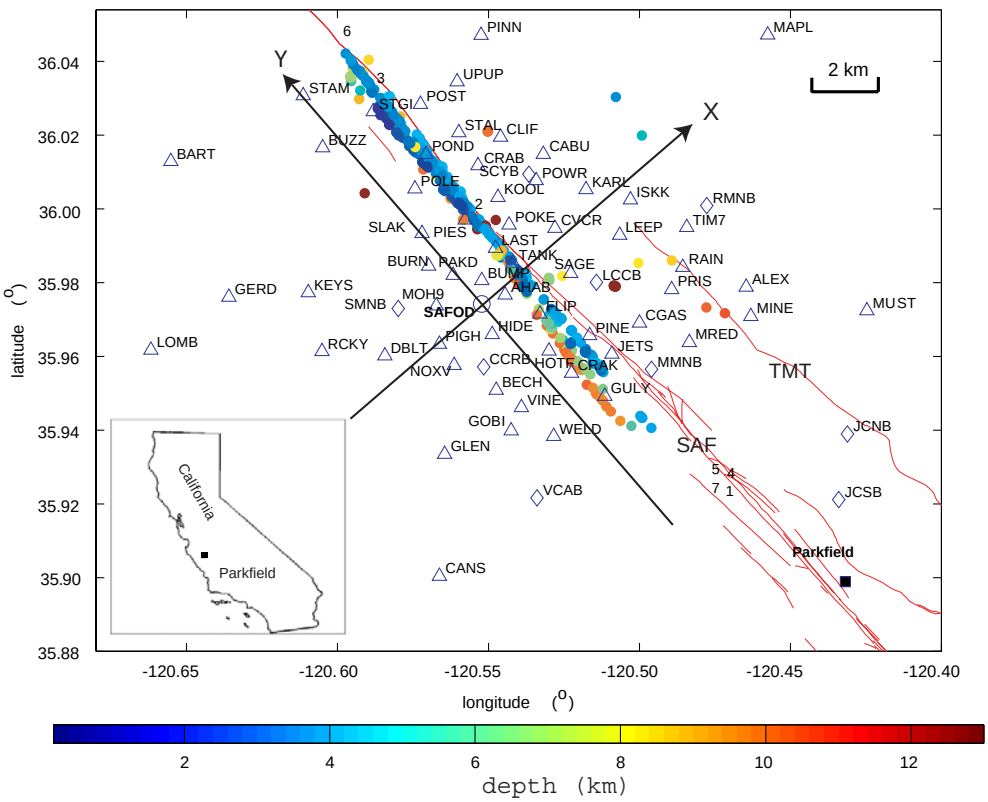


**Figure 1** A location map of the study region. The surface trace of the SAF and nearby faults are represented by red lines. Triangles and diamonds indicate station locations of PASO and HRSN, respectively. Solid circles show hypocentral locations of the events. Solid circles show hypocentral locations of the events. Their colors are associated with the event depths. Numbers indicate the cluster locations. A fault parallel coordinate used for data analysis is indicated in the figure with arrows.

Our study area is located near the town of Parkfield in central California (Fig. 1), along a segment of the SAF that fails through a combination of aseismic creep and regularly recurring microearthquakes. The Parkfield fault segment is recognized as the transition zone between the 170-km-long creeping part of the SAF to the northwest and the 300-km-long locked portion of the fault that ruptured during the 1857 great earthquake to the southeast. There were a number of magnitude 6 events, including the 2004 Parkfield earthquake, that occurred in this portion of the fault. The geological features in the area are dominated by the northwest-southeast trend of the right lateral strike-slip plate boundary at the SAF and associated subparallel strike-slip and reverse faults. The Salinian block covered by Tertiary and Quaternary sediments is on the southwest side of the SAF. On the northeast side of the fault, the basement of Franciscan melange is overlain by Cretaceous and younger sediments of the Great Valley sequence. The stress orientations measured in the SAFOD Pilot Hole indicate a rotation of $\sigma_H$ with depth from approximately north-south at the surface to an angle of $70^o$ to the SAF at depth (Hickman & Zoback 2004). The latter is compatible with the measurements of regional $\sigma_H$ (e.g. Townend & Zoback 2004).

## 3 ANALYSIS METHOD AND DATA PROCESSING

Both visual inspection methods and automated methods have been used in SWS analysis. Visual inspection methods (e.g. horizontal particle motion analysis) have problems of subjectivity or observer bias that might affect measurements. However, visual inspection methods are useful for checking results from automatic processing. Automated methods are required to analyze large data sets effectively, in an unbiased and systematic manner. The cross-correlation (CC) method (e.g. Fukao 1984), the covariance matrix (CM) method (e.g. Silver & Chan 1991), and the aspect ratio (AR) method (Shih *et al.* 1989) are three automated methods commonly used in SWS analysis. They can be viewed as eigenvalue-based measures of linearity of particle motion (Silver & Chan 1991). In an ideal situation, all these methods should give identical results. For real data, the analyzed results may vary with the employed method.

In the CC method, the two horizontal seismograms are rotated in the horizontal plane at a $1^o$ increment of azimuth $\alpha$ from $0^o$ to $180^o$. For each azimuth, the cross-correlation coefficient (CCC) between the two orthogonal seismograms is calculated for a range of time delays (TDs) $\tau$ in a selected time window. When the absolute value of the CCC $c(\alpha,\tau)$ reaches a maximum, the corresponding values of $\alpha$ and $\tau$ are chosen as the PD of the fast shear wave (FSW) and the time delay of the slow shear wave (SSW), respectively. The underlying assumption of the CC method is that the fast and slow horizontal components have similar waveforms. However, for local earthquake seismograms, the fast and slow horizontal components may or may not display similar waveforms, as the polarizations respond differently to the structure between source and receiver (Aster *et al.* 1991; Liu *et al.* 1997, Liu *et al.* 2005b). Similar to the CC method, the CM method finds the SWS parameters based on minimizing the smaller eigenvalue of a 2 x 2 covariance matrix constructed from the horizontal-component seismograms. The AR method maximizes the ratio between the larger and smaller eigenvalues of the covariance matrix to determine the fast polarization direction. The ideal window for calculating the AR value should start at the onset of the FSW and end right before the arrival of the SSW. An optimal window is obtained by testing various window lengths.

Once the PD is resolved, the TD is estimated by cross-correlating the FSW with the SSW. The AR method excels in estimating the PD when the TD of the SSW is large (e.g. > 0.1 sec) and signal to noise ratio is high, regardless of the similarity between the fast and slow components (Liu *et al.* 2004). However, we found that the CC method gives much more robust results than the AR method for our data set, in which the S phases are usually contaminated with the coda of the P phases and the TDs between the fast and slow shear waves are usually not very large. Since both the CC method and the CM method perform a grid search over the $\alpha - \tau$ space to find the best solution that produces the most linear particle motion, the CC method and the CM method had very similar results, as expected. Thus, we only present the results from the CC method in the following discussion. Rau et al. (2000) adopted a method based on a two-dimensional normal distribution (Kreyszig 1970) for confidence interval estimation. We use their scheme to estimate the measurement uncertainty with a 95% confidence interval.

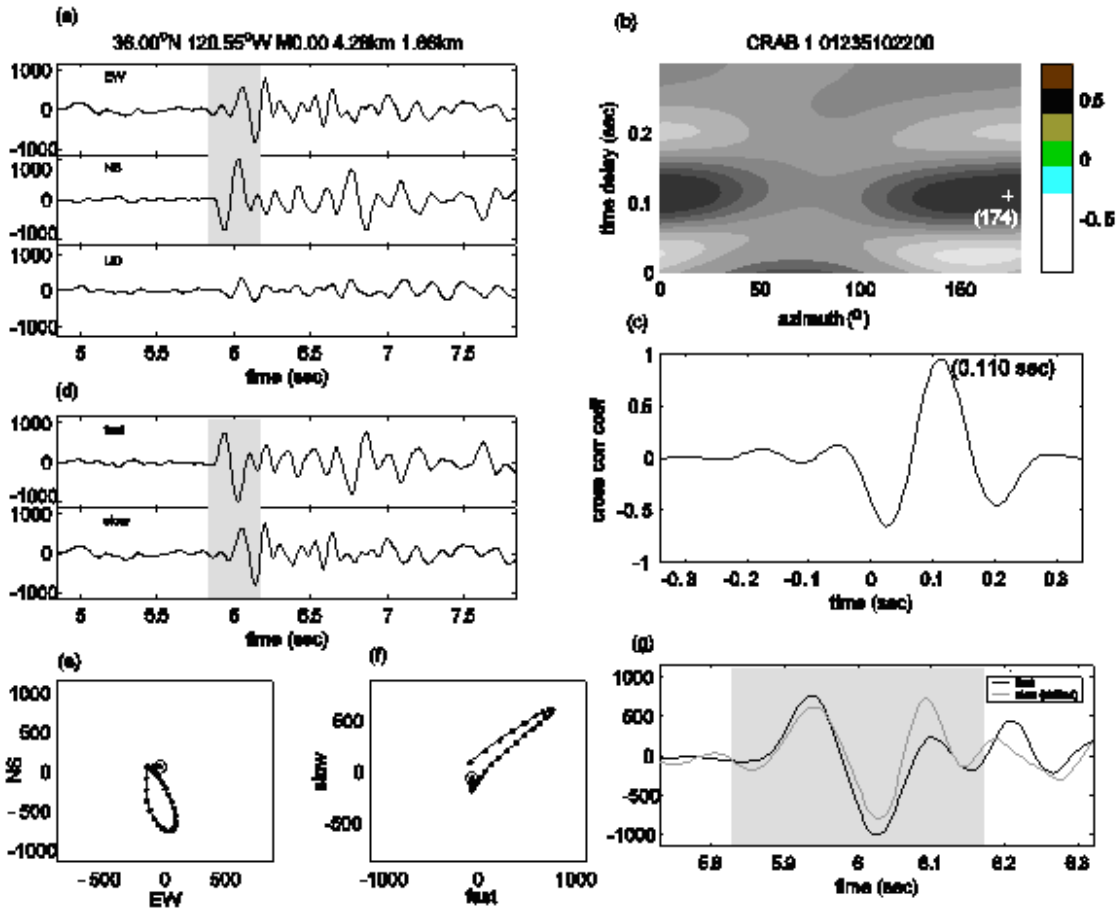


**Figure 2** An example of SWS analysis with the CC method. (a) Original three-component seismograms. (b) A contour plot of the CCC values. The maximum CCC value is indicated by the cross at PD = 174o and TD = 0.11 sec. (c) A slice of (b) at the measured PD. (d) Seismograms rotated to the estimated fast and slow PDs. (e) The horizontal particle motion of the original seismograms. (f) The horizontal particle motion of the fast and slow components shifted with the measured TD. (g) Waveforms of the fast and slow components shifted with the measured TD.

Fig. 2 illustrates the SWS analysis process using the CC method. The original short period 3-component seismograms are given in Fig. 2a. The shaded areas indicate the time window for SWS analysis. A contour plot of the CCC values is shown in Fig. 2b. The maximum CCC value is indicated by the cross and its corresponding azimuth and time delay give the PD (here $174^o \pm 16^o$) and the TD (here $0.110 \pm 0.020$ sec). Fig. 2c is a slice through Figure 2b at the determined PD. Fig. 2d shows the horizontal component waveforms rotated into the determined PDs of the FSW and the SSW. Fig. 2e shows the horizontal particle motion of the original seismograms. As a check, we advance the SSW with the estimated TD and show the resulting horizontal particle motion and the shifted seismograms in Figs 2f and 2g, respectively. The linear particle motion in Figure 2f and well-matched seismograms in Figs 2g indicate that the above measurement is valid.

An ideal time window for shear wave splitting analysis should begin right before the fast arrival and end after the slow arrival. Peng & Ben-Zion (2004) chose an optimal window by sliding a 0.6-s time window around the fast S arrival to account for the picking errors of the S arrivals. However, the analysis window in such a method may include a significant portion of waveform before the S arrival, thus the P coda could affect the SWS measurements. Since our data set has excellent S picks and picking error is generally below 0.02 sec, we fixed the start of the window at 0.02 sec before the S arrival pick. A suitable end point for the window may vary with different seismograms with different time delays and different shear wave properties. Thus, we use a variable length window to determine the end position that gives the maximum CCC value between the fast and slow components. The fast and slow components may match best at a certain window length when one of the two components skips a cycle. This will lead to erroneous measurements of SWS parameters. However, searching the maximum value over a space of three parameters $\alpha$, $\tau$ and window length provides an effective way to reduce the possibility of cycle skipping.

The S-P wave conversion at the ground surface will affect SWS measurements. Its effect can be avoided by using steep rays within the shear-wave window (i.e., rays with incidence angles less than $i_0 = \sin^{-1}(V_s / V_p)$ (Nuttli, 1961)). The average $i_0$ calculated from an updated local velocity model of Thurber *et al.* (2004) is about $43^o$. Considering the high velocity gradient near the surface, we use data with epicentral distance less than the focal depth. The calculated incidence angles confirm that the rays corresponding to the event-station pairs conforming to this criterion are well within the estimated shear-wave windows.

Prior to the analysis, the seismograms are band-pass filtered at 1-10 Hz using a two pole, one pass Butterworth filter. Most of the original seismograms are sampled at 100 samples per sec (sps) but some are recorded at 250 sps. Therefore we interpolated the data to 200 sps to form a homogenous data set for SWS analysis.

We use the following criteria similar to some of those used by Peng & Ben-Zion (2004) to ensure reliability of the results. 1) The CCC value between the fast and slow component is larger than 0.75. 2) The signal-to-noise ratio (SNR) is larger than 2.5. The SNR is measured from the ratio of the averaged amplitude in the SWS analysis window to that in a 0.2 sec window before the S arrival. 3) The change of the measured TD is less than 0.02 sec when the window size is varied by $\pm$ 0.02 sec. 4) The change of the measured fast polarization direction is less than 10 degrees when the window size is varied by $\pm$ 0.02 sec. Criterion 1) is to ensure similarity between the fast and slow shear waves.

Criterion 2) is to eliminate data with a suspected contamination by the P coda. Criteria 3) and 4) guarantee that the measured results are insensitive to the window size. This is required for a robust analysis of SWS. Obviously, there is a trade off in data quality versus data quantity. The cut-off value for each criterion was chosen to be compatible with previous studies and also to make sure that the majority of measurements remain. For instance, a high CCC threshold can ensure that the measured results are reliable, but it may result in loss of some useful measurements in case the fast and slow shear waves are not sufficiently similar.

## 4 THE SPATIAL DISTRIBUTION OF ANISOTROPY

### *4.1 The polarization direction of the fast shear wave*

The splitting of a shear wave can occur anywhere along the ray path. It is not an easy task to map the spatial distribution of anisotropy from the observed SWS parameters. Rose diagram statistics of the PDs for each station have commonly been used to analyze the distribution of the measured PDs. Fig. 3 shows such rose diagrams for the measured PDs for all 67 stations. As shown in Fig. 1, the events are mainly located within the SAF zone. Stations away from the SAF have only a few deep events within the shear wave window. Most stations have scattered PD measurements. To analyze consistency of the measured PDs at each station quantitatively, we applied the Von Mises method to calculate the mean PD $\overline{\alpha}$ and the mean resultant length $\overline{R}$ (Mardia & Jupp 2002; Cochran *et al.* 2003). $\overline{R}$ varies between 0 and 1 and is an inverse analogue of the variance. $\overline{R} = 1$ corresponds to a totally aligned distribution, whereas $\overline{R} = 0$ can arise in very different ways, such as with a uniform circular distribution or with clusters of values 180$^o$ apart. The method is suitable for circular data ranging from 0$^o$ to 360$^o$. Since the polarization directions are normally defined from 0$^o$ to 180$^o$, we doubled the measured PDs to form a circular data set. The following equations 1 - 4 show steps in the calculations of $\overline{\alpha}$ and $\overline{R}$ for *N* measurements,

$$S = \sum_{i=1}^{N} \sin(\alpha_i), \tag{1}$$

$$C = \sum_{i=1}^{N} \cos(\alpha_i), \tag{2}$$

$$\overline{\alpha} = \tan^{-1}(S/C), \text{ and} \tag{3}$$

$$\overline{R} = \sqrt{S^2 + C^2}/N. \tag{4}$$

We list the calculated $\overline{\alpha}$ , $\overline{R}$ and sample size N along with the mean TD and the associated standard deviation for all stations in Table 1.

There are 13 stations for which the measured PDs are well clustered in a single direction (with $\overline{R}$ > 0.65). Of them, STGI, POLE and AHAB are right on the southwest side of the SAF. The mean PDs for these stations are around 100$^o$. NOXV and ALEX are located on the southwest and northeast sides of the fault, respectively, and both are several kilometers away from the fault. Their mean PDs are approximately parallel to the SAF trace. SLAK, CANS, SMNB, RCKY and GLEN are located on the southwest side of the fault and their mean PDs are nearly in a north-south orientation. RMNB, RAIN and PRIS

are located near ALEX. However, their mean PDs vary significantly. Among the stations with lower $\overline{R}$ values (< 0.4), many are located along the fault, namely LAST, TANK, POND, KOOL, CVCR, HOTF, PIES, CRAB, SAGE, PINE, POKE, and PAKD. The rest of the stations with medium $\overline{R}$ values (0.4 -0.65) are distributed through the area. The rose diagram in the lower left corner of Fig. 3 shows the distribution of all the 5627 PD measurements. There are two notable peaks in the rose diagram. One is around 110°, subparallel to the SAF, and the other is around 170°, approximately parallel to $\sigma_H$ measured from the SAFOD Pilot Hole near the surface. These two peaks likely correspond to the two possible major sources of the anisotropy in the area: fault zone related structural fabric and stress induced alignment of cracks (Boness & Zoback 2004, 2006). We note that the regional $\sigma_H$ and the measured $\sigma_H$ from the SAFOD Pilot Hole at depth are oriented NNE. It is possible that the shallow crustal structure affects the orientations of the measured PDs more than the deeper structure. As we can see from Fig. 3, a significant amount of the measured PDs are different from either the SAF strike or the $\sigma_H$ direction. This illustrates the complexity of anisotropy in the area. The localized anisotropy structure and the mixed anisotropy mechanisms might be responsible for the scattered PD distribution.

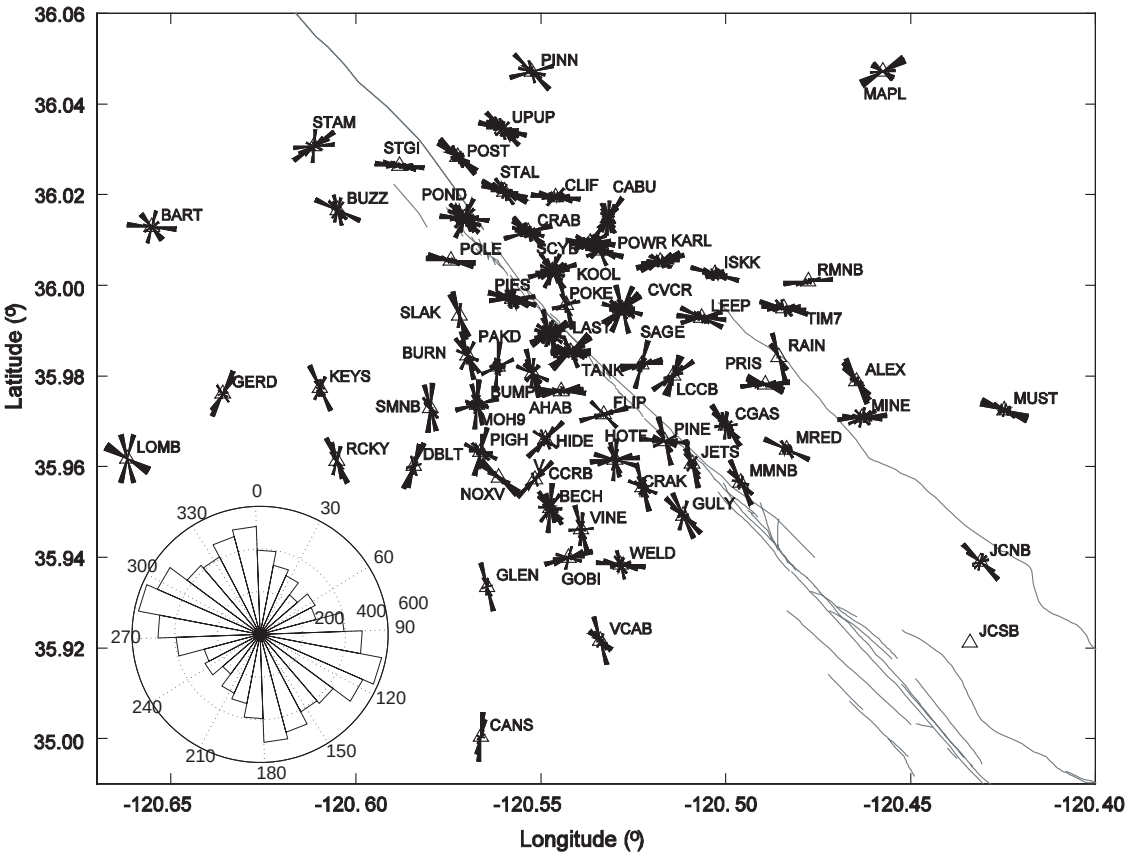


**Figure 3** Rose diagrams showing the PDs of the fast shear wave as recorded by each station. The rose diagram in the lower left corner shows the distribution of all the PD measurements.

**Table 1**. Statistics of the PDs and TDs for each station. $\overline{R}$ is the mean resultant length of PDs, Std is the standard deviation of TDs, and N is the sample size.

| Station | DP(°) | $\overline{R}$ | TD(s) | Std | N | Station | DP(°) | $\overline{R}$ | TD(s) | Std | N |
|---|---|---|---|---|---|---|---|---|---|---|---|
| SLAK | 176 | 0.87 | 0.021 | 0.019 | 138 | UPUP | 134 | 0.44 | 0.055 | 0.045 | 99 |
| RAIN | 165 | 0.86 | 0.036 | 0.038 | 64 | STAL | 132 | 0.43 | 0.077 | 0.048 | 229 |
| NOXV | 138 | 0.81 | 0.078 | 0.045 | 138 | STAM | 58 | 0.42 | 0.047 | 0.039 | 32 |
| CANS | 25 | 0.79 | 0.041 | 0.035 | 19 | POST | 140 | 0.42 | 0.083 | 0.046 | 153 |
| PRIS | 108 | 0.78 | 0.123 | 0.059 | 60 | FLIP | 99 | 0.41 | 0.047 | 0.051 | 68 |
| SMNB | 176 | 0.76 | 0.024 | 0.017 | 119 | MINE | 93 | 0.40 | 0.039 | 0.039 | 24 |
| RCKY | 176 | 0.75 | 0.048 | 0.040 | 47 | LOMB | 154 | 0.40 | 0.077 | 0.026 | 4 |
| GLEN | 2 | 0.75 | 0.028 | 0.024 | 41 | CABU | 17 | 0.40 | 0.064 | 0.052 | 148 |
| RMNB | 90 | 0.73 | 0.085 | 0.046 | 19 | BUZZ | 157 | 0.40 | 0.040 | 0.046 | 40 |
| POLE | 111 | 0.69 | 0.056 | 0.059 | 180 | POWR | 110 | 0.39 | 0.072 | 0.051 | 162 |
| STGI | 107 | 0.68 | 0.080 | 0.039 | 139 | JCNB | 139 | 0.39 | 0.048 | 0.053 | 8 |
| ALEX | 154 | 0.68 | 0.098 | 0.053 | 52 | CGAS | 155 | 0.39 | 0.077 | 0.061 | 62 |
| AHAB | 97 | 0.66 | 0.041 | 0.032 | 110 | PINN | 126 | 0.37 | 0.063 | 0.050 | 50 |
| DBLT | 29 | 0.62 | 0.053 | 0.028 | 78 | ISKK | 101 | 0.37 | 0.059 | 0.055 | 39 |
| BURN | 174 | 0.62 | 0.053 | 0.053 | 237 | MRED | 125 | 0.36 | 0.070 | 0.058 | 17 |
| TIM7 | 116 | 0.61 | 0.079 | 0.064 | 46 | BECH | 172 | 0.36 | 0.054 | 0.033 | 101 |
| MUST | 118 | 0.61 | 0.102 | 0.058 | 15 | CRAB | 117 | 0.35 | 0.059 | 0.044 | 199 |
| KEYS | 6 | 0.61 | 0.077 | 0.053 | 20 | SAGE | 65 | 0.33 | 0.045 | 0.035 | 35 |
| VCAB | 158 | 0.60 | 0.036 | 0.028 | 29 | PINE | 132 | 0.30 | 0.072 | 0.049 | 11 |
| LCCB | 44 | 0.60 | 0.076 | 0.054 | 71 | TANK | 93 | 0.28 | 0.042 | 0.035 | 215 |
| LEEP | 109 | 0.56 | 0.069 | 0.069 | 76 | BART | 136 | 0.28 | 0.045 | 0.042 | 12 |
| MMNB | 157 | 0.55 | 0.073 | 0.050 | 61 | POKE | 12 | 0.27 | 0.030 | 0.039 | 78 |
| CCRB | 50 | 0.55 | 0.025 | 0.022 | 82 | HIDE | 35 | 0.24 | 0.071 | 0.042 | 50 |
| GULY | 149 | 0.50 | 0.069 | 0.047 | 23 | WELD | 121 | 0.23 | 0.029 | 0.027 | 92 |
| SCYB | 99 | 0.49 | 0.066 | 0.048 | 193 | HOTF | 172 | 0.22 | 0.065 | 0.046 | 54 |
| MAPL | 93 | 0.49 | 0.081 | 0.068 | 8 | PIES | 124 | 0.21 | 0.073 | 0.054 | 222 |
| JETS | 169 | 0.49 | 0.061 | 0.061 | 28 | PIGH | 154 | 0.19 | 0.084 | 0.063 | 93 |
| KARL | 94 | 0.48 | 0.084 | 0.051 | 141 | POND | 126 | 0.14 | 0.076 | 0.054 | 193 |
| BUMP | 173 | 0.48 | 0.039 | 0.032 | 57 | PAKD | 14 | 0.12 | 0.045 | 0.056 | 91 |
| GOBI | 84 | 0.47 | 0.045 | 0.032 | 86 | MOH9 | 14 | 0.12 | 0.053 | 0.046 | 131 |
| GERD | 30 | 0.47 | 0.068 | 0.049 | 15 | CVCR | 59 | 0.09 | 0.064 | 0.056 | 116 |
| CLIF | 99 | 0.47 | 0.075 | 0.046 | 168 | KOOL | 84 | 0.08 | 0.060 | 0.044 | 171 |
| CRAK | 165 | 0.46 | 0.044 | 0.033 | 66 | LAST | 87 | 0.03 | 0.055 | 0.038 | 126 |
| VINE | 1 | 0.44 | 0.028 | 0.024 | 56 | | | | | | |

*4.2 The ray paths*

Due to local extreme velocity contrasts across the fault (Thurber *et al.* 2004, 2006), it is expected that the ray paths in the area will be accordingly very complicated. To analyze the measured SWS parameters in detail, accurate knowledge of the ray paths is important. Fortunately, the study region has a high quality, high resolution crustal velocity model. We calculate the ray paths based on an updated version of the Thurber *et al.* (2004) model and the corresponding event locations and show the results for three representative stations in Fig. 4. We also plot slices through the shear velocity model in the figure. The large velocity contrast across the fault frequently results in rays bending to the southwest

side of the SAF where the velocity is higher. As shown in Fig. 4a, for station BURN located about 2 km southwest of the SAF, the rays from some deep events approach the station from the southwest side of the station, even though these events are located within the SAF zone to the northeast. POST is right at the northeast side of the fault. The deep rays also bend to the other side of the fault (Fig. 4b). Much less bending occurs for the rays propagating to SCYB, a station located 2 km northeast of the fault (Fig. 4c). The color of each ray in the figures represents the TD associated with the ray path. As is evident from the figures, groups of nearby rays often have similar colors; however, the measured TDs vary greatly for rays propagating through different crustal regions.

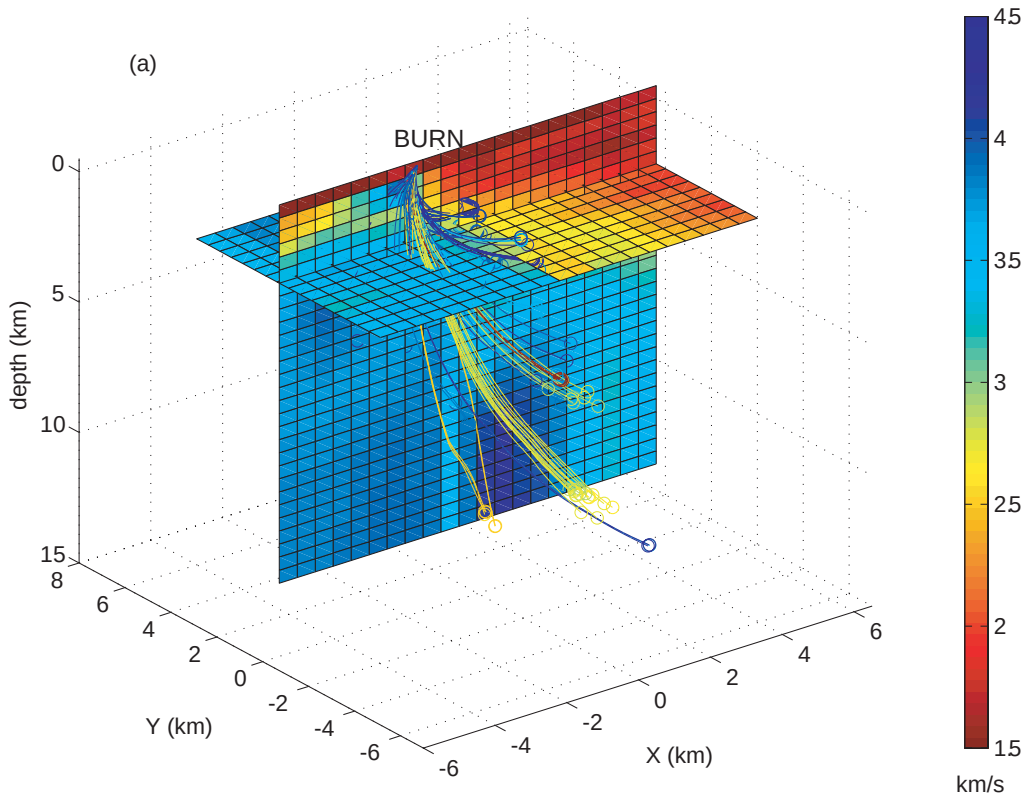


**Figure 4** The calculated ray paths for three stations and the shear velocity model. a) Station BURN. b) Station POST. c) Station SCYB. Color bars give the shear velocity scale. The color of each ray represents the time delay associated with the ray path with the "jet" color scale. The red color is related to 0.2 sec time delay or higher and the blue color represents zero time delay. Note that most of the events are within the fault zone located near a vertical plane X = 1.7. (Figure 4b and c are shown in next page.)

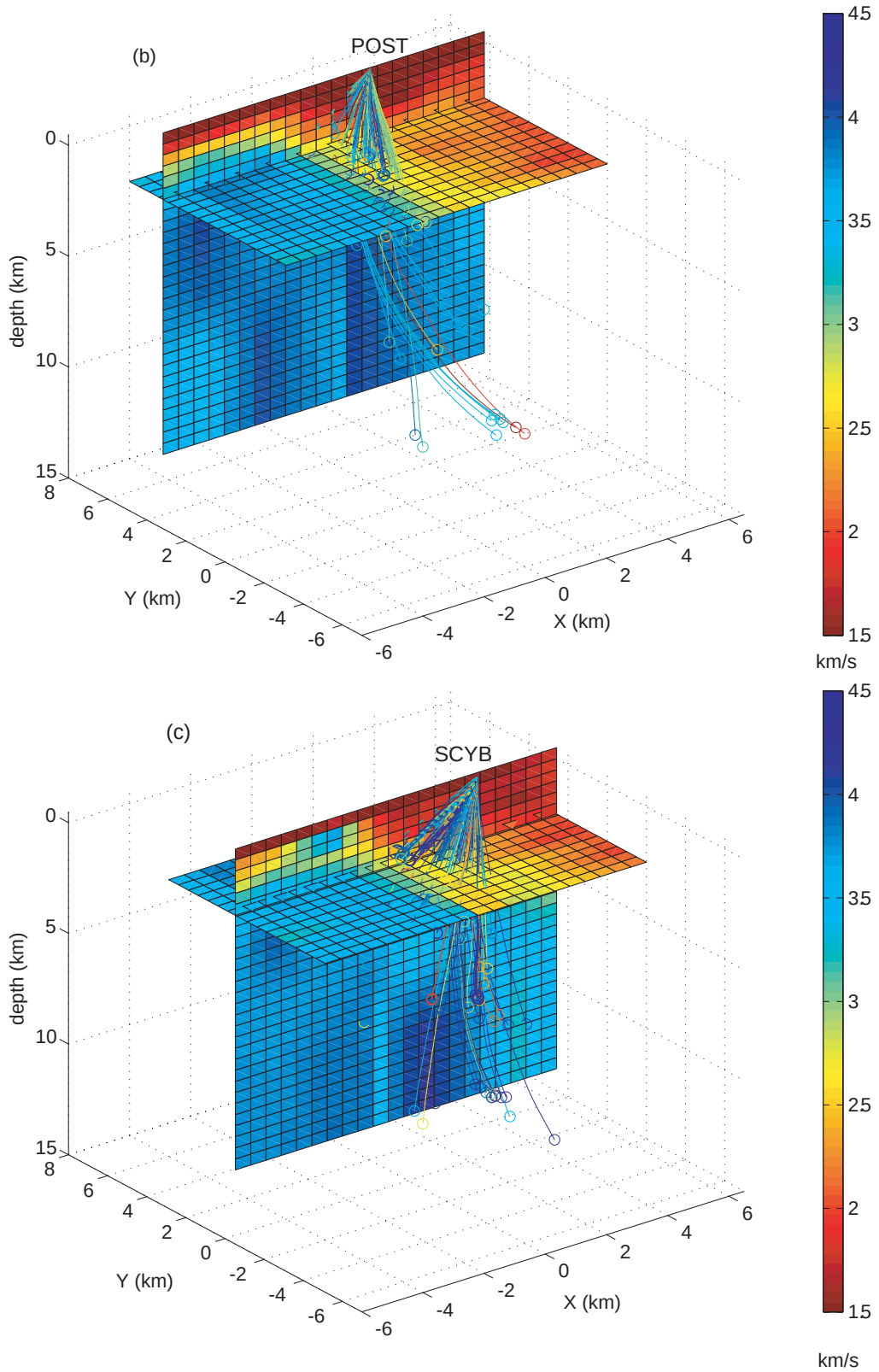


**Figure 4 (continued).**

*4.3 Lateral distribution of polarization direction and time delay*

There are several ways of data presentation used to look for systematic patterns in the measured SWS results. Cochran *et al.* (2006) plotted PDs at earthquake locations or station locations and found no coherent patterns present in either plot. As discussed in the previous section, the distributions of PDs are scattered for most of the stations. This indicates that the near-station region does not completely dominate the measured PDs. It is very likely that both the PD and TD are dependent on the path, that is, which part of the region is sampled by the ray. An alternative way commonly used to display data is to plot the SWS parameters at the midway point between the source and station. However, as pointed out in the previous section, the ray paths often bend severely from the straight lines linking the sources and stations. Thus, this method will result in a false representation of the spatial character of the SWS measurements. For this reason, we use a different strategy of data presentation to account for the complexity of the ray paths in the area. We plot the SWS parameters at the positions where the rays intersect with horizontal sections at different depths to search for systematic patterns in the data, as shown in Fig. 5.

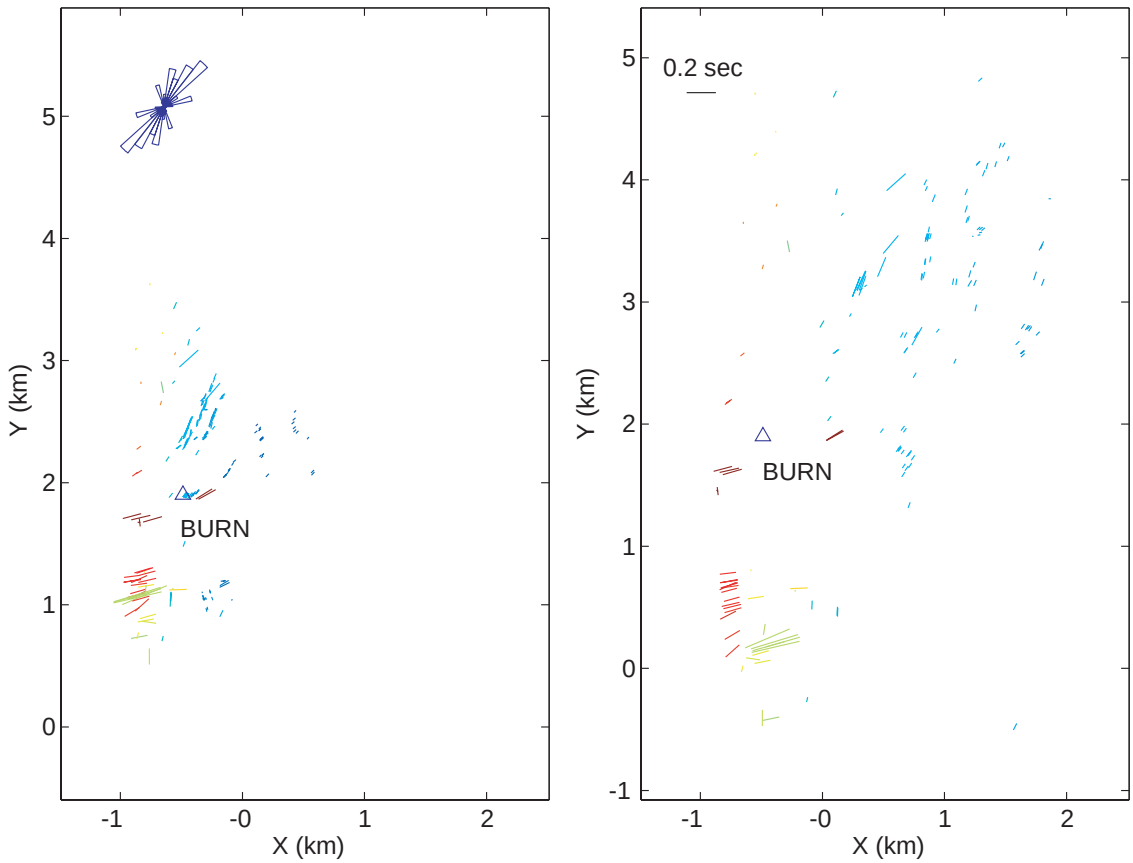


**Figure 5** Plots of the SWS parameters for station BURN. Bars are orientated parallel to the PDs and scaled to the TDs. Each bar is placed at the point where the ray intersects with the 1.5 km deep section (left) or 3 km deep section (right). The colors of the bars are related to the event depths with the same color scale as that in Figure 1. Note that Y–axis is oriented along the SAF strike.

Fig. 5 shows such a plot for station BURN. Bars in the figure are oriented parallel to the PDs and scaled to the TDs. The color of each bar is related to event depth with the color scale shown in Fig. 1. The left and right panels of the figure correspond to depths of 1.5 km and 3 km below sea level, respectively. The orientations of the PDs for BURN are moderately scattered with an $\overline{R}$ value of 0.62. From the figure, it is evident that a clear spatial pattern exists for both the PDs and TDs in the 1.5 km section. The features are more coherent in the 3.0 km section. The measured PDs associated with ray paths that sample the region northeast of the station are generally oriented at small angles to the SAF, while those associated with ray paths that sample the area southwest of the station are nearly perpendicular to the SAF. The former group of measurements has much smaller TDs than the latter group. The difference in TDs between these two groups of measurements could be related to both their different ray lengths and different anisotropy strengths along their ray paths. Considering the significant differences between these two groups of measurements both in PDs and TDs, the lateral variation of anisotropy must be substantial in the area. This is also supported by the observation that the measured TDs associated with ~7 km deep events (green bars) are much larger than those associated with ~11 km deep events (red bars). As shown in Figs 4a and 5, the ray paths from 1.5 km below sea level to the station elevation of ~ 0.5 km sample a small volume of the crust beneath the station. It is unlikely that there is a dramatic change of anisotropy both in orientation and intensity within such a small domain. However, the ray paths from 1.5 km to 3.0 km or deeper propagate through a relatively extensive volume, which is more feasible to accommodate a strong variation of anisotropy. Thus it is likely that there is pervasive anisotropy in this part of the region.

To illustrate the lateral distribution of anisotropy in the study area, we plot the measurements for all stations in Fig. 6a using gray bars in a similar way as in Fig. 5. Each gray bar is located at the position where the ray goes through the 1.5 km deep horizontal section. An area could be sampled by various ray paths related to different event-station pairs. The scatter in both the orientations and lengths of the bars in some areas is expected, since both the corresponding PD and TD could be also affected by the other region that the ray propagates through, but it is evident that there are some coherent patterns in the plot. We averaged the measurements on grid points (0.5 km by 0.5 km) and plot the results in the figure using red bars. The orientation and length of the red bar represent the mean PD and the mean TD, respectively, within an averaging radius of 0.36 km. The averaging radius was chosen to have each measurement counted at least once. Fig. 6b is similar to Fig. 6a except the red bar is scaled to the mean resultant length to show the variance of the PDs. The average $\overline{R}$ in the figure is 0.60. A plot at 2.0 km depth gives very similar patterns with an average $\overline{R}$ of 0.58. Thus the lateral patterns in the plot at 1.5 km depth are slightly more coherent than those in the one at 2.0 km depth. From Figs 6a and 6b, we can see that, in general, the orientations of bars in the region including the SAF zone and the northeast side of the fault are parallel or subparallel to the SAF, while those on the southwest side of the fault are more or less oriented to the direction of $\sigma_H$ in the region; however, there are some regions in which the measurements do not conform to this general pattern. The fault parallel or subparallel PDs around the SAF likely reflect the structural anisotropy due to aligned fault zone fabrics. The Table Mountain (TMT) thrust fault (Fig. 1) located to the northeast of the SAF probably plays a major role in the measurements in the area around the position (4, -4) in the figure. The observed PDs in the area between the

positions (4, -2) and (2, 3) are orientated NW and might be associated with a branch of the TMT fault, which has a similar orientation, starting around station MINE and ending around POST. One of the regions with abnormal orientations of PDs is around the position (-1, 1). The SAF-parallel PDs are significantly different from nearby measurements. A possible interpretation is that they might be related to a concealed fault in the region (Thayer & Arrowsmith, 2005). The other abnormal PDs are observed in the region around the positions (2, 1) and (2, -2). These SAF-normal PDs could be related to the localized anisotropy structure in the region due to aligned sedimentary beds or small faults. From Fig. 6a we can also see that although the average TDs are coherent over a small area, the average TDs vary with different regions and the observed TDs in any given region are scattered as well. Similarly, the average TD for each station (Table 1) changes significantly and its standard deviation is as large as its mean value. We note that some portion of these TD variations should be due to the different ray lengths that the associated event-station pairs have.

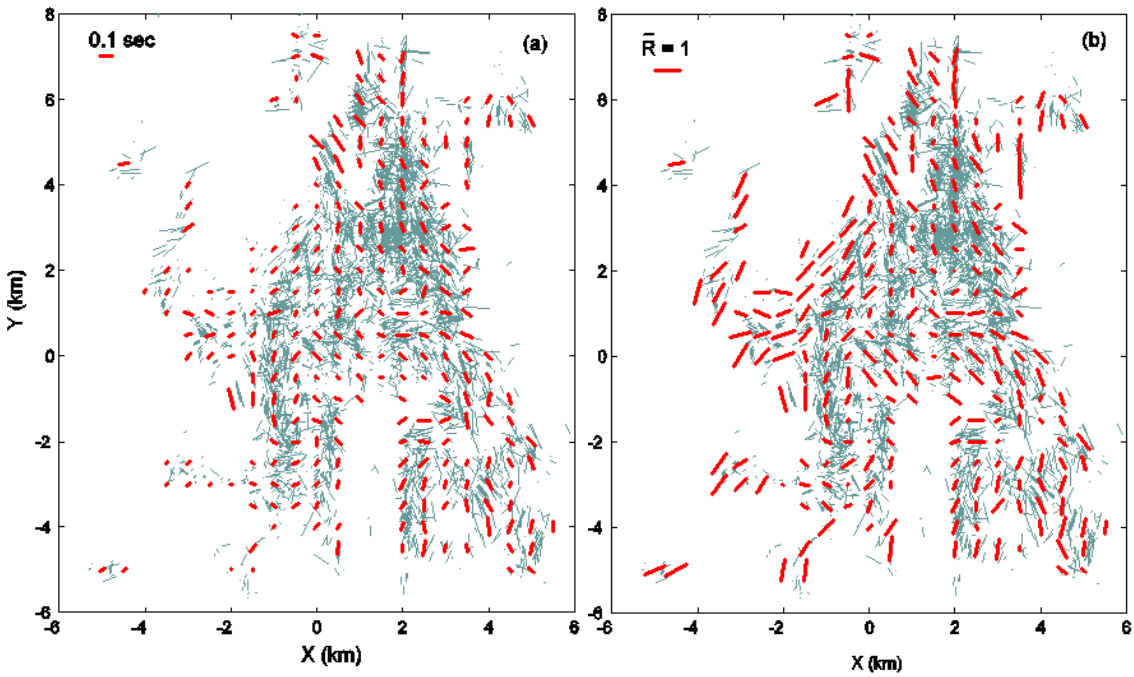


**Figure 6** Plot of the measured SWS parameters for all the stations. Gray bars represents a total of 5627 pairs of PDs and TDs with their orientations and lengths. Each bar is placed at the point where the associated ray reaches 1.5 km depth. (a) Red bars are oriented to the mean PD of measurements within a 0.36 km distance and scaled to the mean TD. (b) Red bars are scaled to the mean resultant length.

### *4.4 Depth extent of anisotropy*

The events used in this study extend from about 1.8 km to 16 km deep. This provides a good opportunity to constrain the depth extent of anisotropy in the upper crust. Fig. 7 shows plots of the measured TDs versus the event depths for four typical stations. The circles in the figure give the average TDs in a 1 km depth interval and the vertical line indicate the associated standard deviations. The measured TDs for stations BURN, CABU

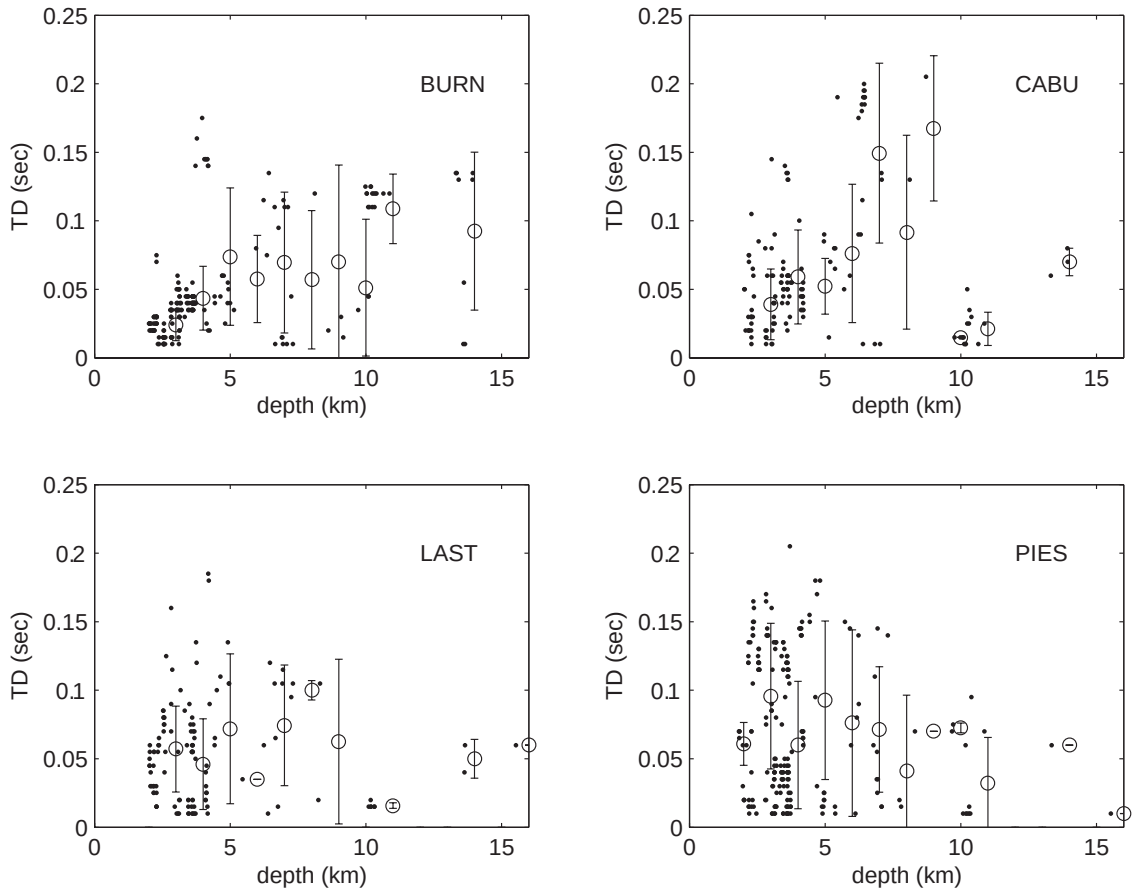


**Figure 7** The measured TDs versus the event depths for four representative stations. Circles give the average TDs in a 1 km depth interval. Bars indicate the standard deviations of TDs.

and LAST display a depth dependence in the depth range ~2 – 8 km, whereas those for station PIES do not. The average TDs for the 1.5 - 2.5 km interval in each subplot illustrate anisotropy strength in the top 2-3 km of the crust beneath the corresponding station. Apparently this portion of the crust beneath BURN has relative week anisotropy. In contrast, for station PIES the measured TDs are dominated by the top 2-3 km of the crust. The large scatter present in all these plots is probably in part due to the strong lateral variations of anisotropy in the study area. We average the measured TDs for all stations within a 1 km interval of depth and show the results in Fig. 8. The average TDs increase from about 0.05 to 0.07 sec from 2 to 7 km in depth, and then fluctuate around 0.06 sec within the depth range of 8-16 km. As indicated in the figure by the vertical bars, the standard deviations of TDs are almost as large as their average values. This is anticipated since we averaged the TD measurements over a region with a strong lateral variation of anisotropy. The systematic depth dependence of the average TDs indicates that the significant anisotropy could extend to 7 km deep. The unexpected observation that the average TDs for the events deeper than 8 km become smaller might be related to the strong lateral variations of anisotropy. We note that there are only about 18% of the TD measurements that are associated with the events deeper than 7 km. Therefore, the

fluctuation of the average TDs in the 8-16 km section could be due in part to small sample size. Including the section from stations to sea level, the top 2-3 km of the crust contributes to about an average value of 0.05sec in TDs. This indicates that, on average, this portion of the crust likely plays a major role in the observed TDs. This should be in part due to the fact that the shear wave also takes a substantial portion of the total travel time in this section of the crust (Liu *et al.* 2004). Shallow crustal anisotropy was also reported by a number of studies in Parkfield (Cochran *et al.* 2006) and other regions (e.g. Zhang & Schwartz 1994; Cochran *et al.* 2003; Peng & Ben-Zion 2004; Liu *et al.* 2004). However, this is a general result obtained by averaging all measurements and the observed anisotropy is apparently much more pervasive in some areas as we discussed before. The substantial anisotropy in some area might extend to as deep as 7-8 km below sea level. There is no evidence that significant anisotropy exists in the depth range 8-16 km below sea level.

In this section we have employed several ways to map the spatial distribution of anisotropy from SWS measurements. The rose diagram statistics for each station can illustrate the orientation of anisotropy well in case SWS is controlled by the shallow structure underneath the given station. Taking into account the complicated ray paths, plots displaying the measured PDs and TDs in the positions where the rays reach at a certain depth appear to give coherent patterns when more pervasive anisotropy contributes to the SWS measurements. The various presentations of the SWS parameters provide a detailed view of spatial distribution of anisotropy in the study area.

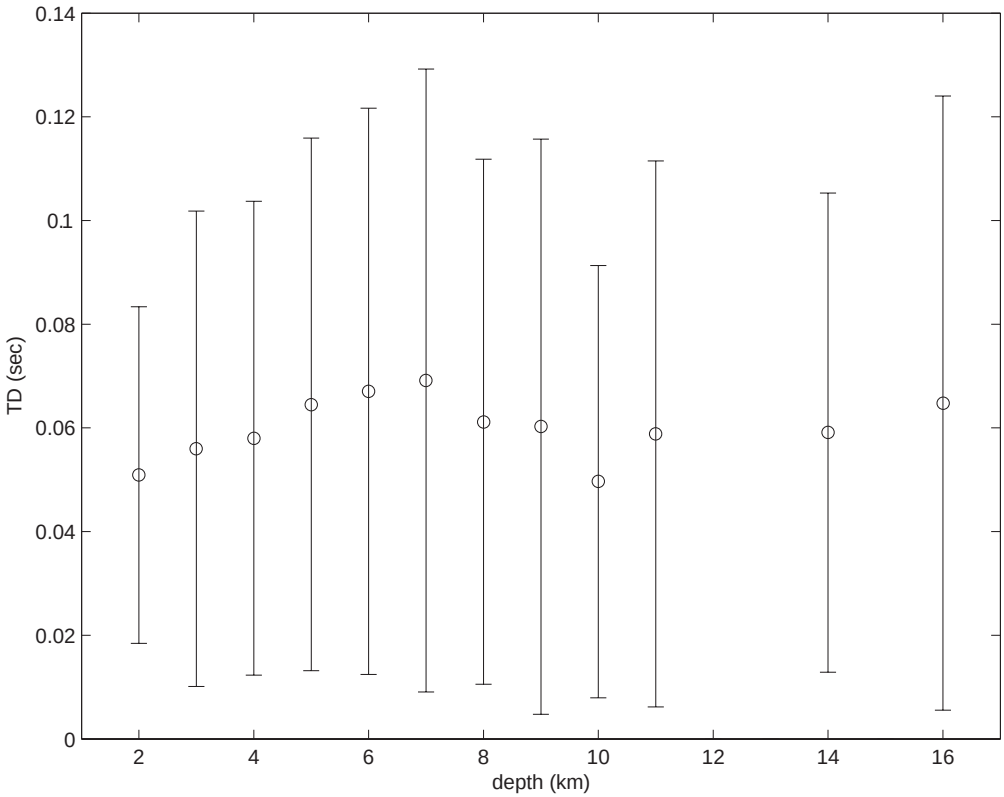


**Figure 8** The average TDs in a 1 km depth interval for all measurements versus depths. Bars give the standard deviations of the measurements.

## 5 THREE-DIMENSIONAL SHEAR-WAVE SPLITTING TOMOGRAPHY

### *5.1 Method*

Above spatial seismic anisotropy analysis can only diagnose the presence of an anisotropic zone somewhere along a ray path and in general cannot define exactly where this zone is located. Assuming weak horizontal anisotropy, Eberhart-Phillips and Henderson (2004) and Ishise and Oda (2005) developed similar anisotropic seismic tomography algorithms to study 3D variations in anisotropy using P-wave first arrivals, in a way similar to Pn tomography where both Pn velocity and anisotropy contribute to the travel time anomalies (Hearn, 1996). Next we present a shear-wave splitting tomography method that directly uses SWS delay times to solve for the 3D distribution of anisotropy percentage. The anisotropic direction is not included in the inversion.

Assuming the SWS results are caused by transverse anisotropy and the measured TDs are accumulated along the ray path (e.g. Crampin, 1991), as follows

$$dt = \int (U_{slow} - U_{fast}) \cos\alpha \, ds \,, \tag{5}$$

where $U_{slow}$ and $U_{fast}$ are slowness parameters for the slow and fast shear waves, α is the angle between the ray path and the vertical direction, and ds is a segment of the ray path. The inclusion of the angle α assures that the contribution of the horizontal component of the ray paths to the shear-wave splitting TDs is zero. We can characterize the strength of anisotropy according to the isotropic slowness U, using an anisotropic coefficient K as follows,

$$K = \frac{U_{slow} - U_{fast}}{U} = \frac{(V_{fast} - V_{slow})V}{V_{fast} V_{slow}} \approx \frac{V_{fast} - V_{slow}}{V} \,, \tag{6}$$

where $V$, $V_{fast}$, and $V_{slow}$ are the isotropic, fast and slow velocities, respectively. This definition of anisotropic coefficient K is slightly different from that in Tadokoro et al. (1999), who defined it as $(V_{fast}-V_{slow})/V_{fast}$. By inserting Equation (6) into Equation (5), we obtain

$$dt = \int KU \cos\alpha \, ds = \int \frac{K \cos\alpha}{V} ds \,. \tag{7}$$

In the following figures, we use $K \times 100$, known as the degree of anisotropy or the anisotropy percentage (Tadokoro et al., 1999), to characterize the anisotropy structure.

Once the earthquake locations and shear wave velocity model are determined from seismic tomography using first S arrival times, Equation (7) represents a linear relationship between shear-wave splitting delay times and anisotropy percentage K. The shear wave velocity model from seismic tomography provides a good approximation of the isotropic velocity model. Therefore, we can directly solve Equation (7) without using iterative methods since it is linear in K. This strategy has the advantage that the final model does not depend on the starting model. Since the K is a nonnegative variable, we solve Equation (7) using the non-negative least-squares (NNLS) solver of Lawson and Hanson (1974).

To stabilize the system of Equation (7), we apply a first-order differencing operator to neighboring anisotropy percentage parameters and apply damping to the whole system.

The optimum weighting and damping parameters are chosen using trade-off curves between model variance and data variance.

*5.2 Data and Inversion Details*

From the SWS analysis results, we only choose TDs that are greater than 0.01 s with CC coefficients greater than 0.75 for anisotropy tomography. When the angle between the shear-wave polarization direction and the fast shear wave direction is too small, the amplitude of the slow shear wave become very small and it is hard to differentiate it from the noise (Zhang and Schwartz, 1994). As a result, there is no shear-wave splitting measured from the records and the zero time delays are just artifacts of this process. For this reason, we do not include zero or very small time delays in our inversion. We select 5636 delay times in total, among which 51% are distributed from 0.01 s to 0.05s, 27% from 0.05 s to 0.10 s, 17% from 0.10 s to 0.15 s, and 6% from 0.15 s to 0.25 s.

The coordinate system origin is located at the SAFOD Pilot Hole (35$^{o}$58.4522' N, 120$^{o}$33.1285') with the Y-axis aligned with the SAF surface trace (40$^{o}$ counterclockwise from north). In the X direction, the inversion grid nodes are positioned at -6.0, -3.0, -1.0, 0.0, 1.0, 2.0, 3.0, 5.0, 7.0, and 10.0 km, and in the Y direction at -8.0, -6.0, -4.0, -2.0, -1.0, 0.0, 1.0, 2.0, 4.0, 6.0, and 8.0 km (Figure 1). In the Z direction, nodes are positioned at -0.5, 0.0, 0.5, 1.0, 1.5, 2.0, 3.0, 4.0, 7.0, and 10.0 km relative to sea level. The shear wave velocity model and event locations are from an updated double-difference tomography inversion of the local earthquake and shot data around SAFOD (Thurber et al., 2004).

We select optimum smoothing weight and damping parameters using trade-off curves of data variance and model variance. The optimum smooth weighting parameters are 1.5 (in all directions) and the optimum damping is 45. The CC coefficients for the delay times are used as data weighting. Because of the possibility of cycle skipping, we slightly down-weight large delay times using a bi-weight function (Waldhauser and Ellsworth, 2000). The weighted RMS time delays are 63.7 ms and after the inversion, the weighted RMS residuals are 36.8 ms.

We analyze the resolution of the model using diagonal resolution and derivative weight sum (DWS) values. During the inversion, only inversion grid nodes whose DWS values are greater than 5 are inverted. Previous studies indicate that DWS distribution is a good qualitative indication of the model resolution (Zhang and Thurber, 2007). For this relatively small problem, we are able to estimate the singular values and vectors of the sensitivity matrix. Because of the smoothing weight used in the inversion that links the neighboring nodes, we see relatively large off-diagonal elements in the full resolution matrix. If we do not use smoothing constraints in the inversion to stabilize the problem, the resulting model will over fit the data that inherently contain strong noise components.

*5.3 Results*

Figures 9 and 10 show the horizontal slices of the anisotropy percentage model at depths of 0 and 2 km and across-fault cross-sections at Y=4, 2, 0, -1, -2, and -4 km. To the southwest of the SAF, shallow tertiary marine sedimentary rocks overlie cretaceous granitic basement rocks. High anisotropic anomalies (>2%) are imaged that are likely due to the preferential closure of fractures in granitic rocks due to an anisotropic stress state

(Boness and Zoback, 2004; 2006; Holmes et al., 2000). Fast polarization directions at stations in this region are consistent with the horizontal maximum compressive stress (Fig. 1). The degree of anisotropy decreases from ~4% at the surface to ~2% at a depth of ~5 km. This may result from increased confining pressure with depth that tends to close fractures in all directions and thus shear anisotropy is less sensitive to the stress (Boness and Zoback, 2006).

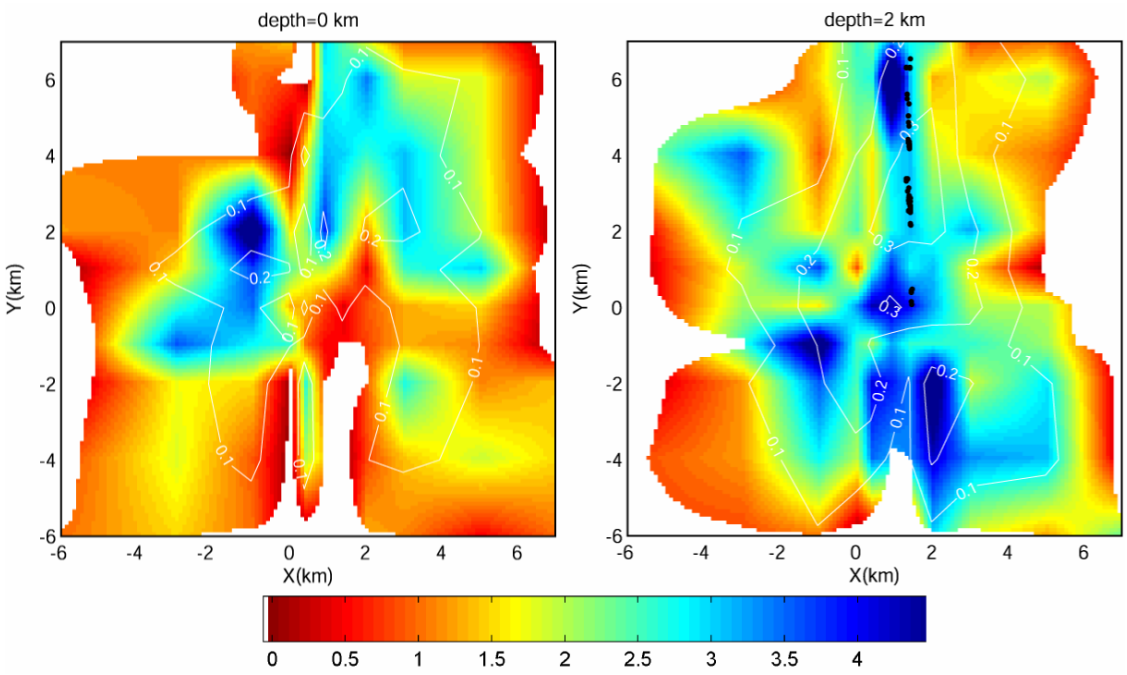


**Figure 9** Horizontal slices of anisotropy percentage model at depths of 0 and 2 km. White contours represent diagonal resolution values. Black dots are earthquakes projected within 0.5 km of the current depth.

For the cross-sections to the southeast of SAFOD (Y=0, -1, -2, and -4 km), there is a highly anisotropic zone northeast of the SAF with anisotropy percentage of 2% to 5% at a depth interval of ~2 to ~5 km. For the zones above and below this highly anisotropic body, the degree of seismic anisotropy is relatively low. This highly anisotropic body corresponds very well to the serpentinite body found by McPhee et al. (2004) in their potential field and geological studies around SAFOD. Laboratory experiments show that serpentine is a highly anisotropic mineral at low pressures due to a strong lattice preferred orientation (LPO) of the major mineral phase antigorite (Kern et al., 1997). This serpentinite body is sandwiched between two masses of Franciscan rock consisting of a heterogeneous mélange of mainly greywacke, shale, greenstone and chert, which are relatively isotropic (McPhee et al., 2004; Okaya et al., 1995). For the cross-sections (Y=2 and 4 km) to the northwest of SAFOD, highly anisotropic anomalies begin to appear at the surface (Figures 9 and 10).

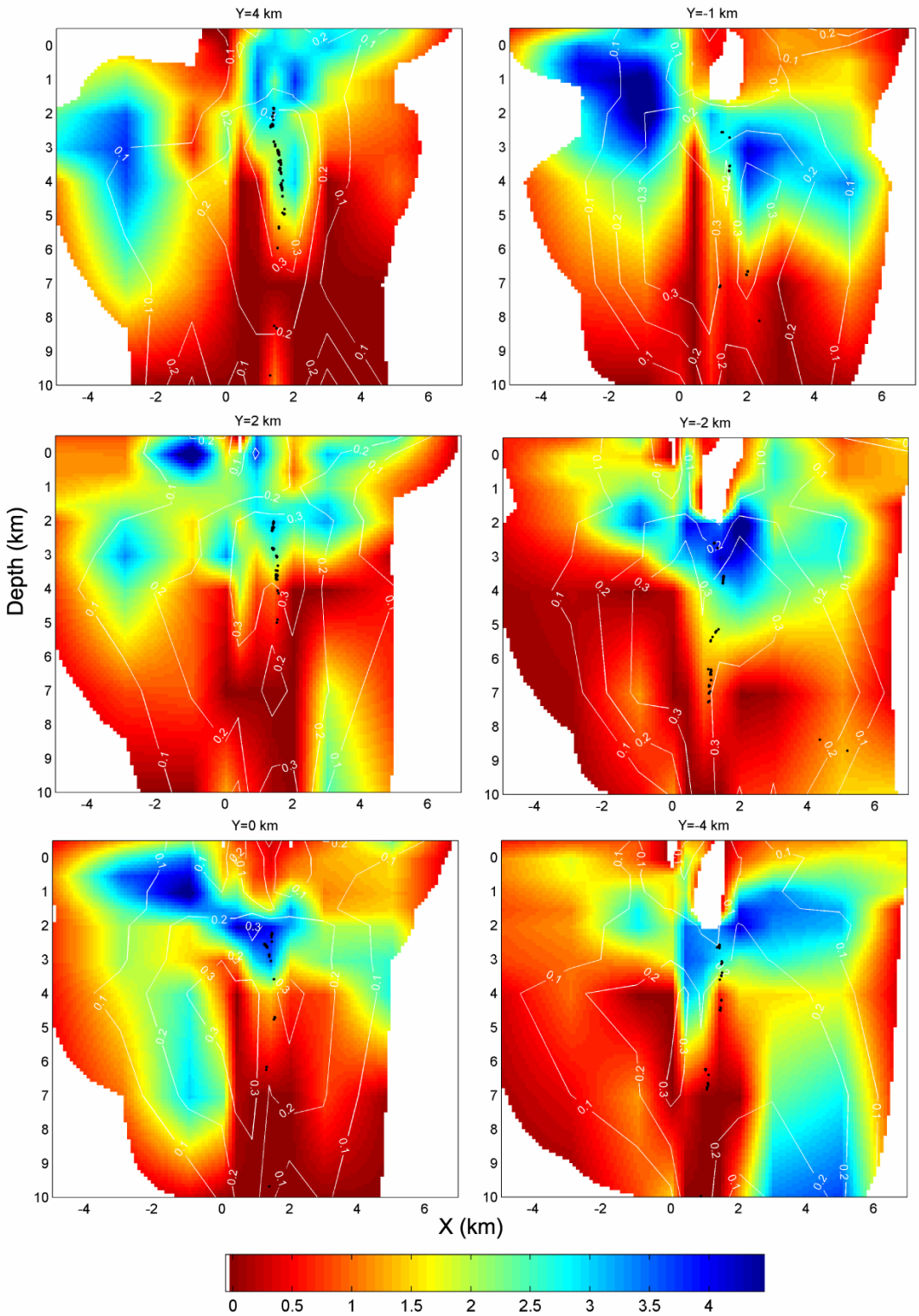


**Figure 10** Across-fault cross-sections of anisotropy percentage model at Y=4, 2, 0, -1, -2, and 4 km. White contours represent diagonal resolution values. Black dots are earthquakes that projected within 0.5 km of the section.

For the cross-section at Y=0 km through SAFOD, the zone between the SAFOD borehole (at X=0 km) and the SAF trace (at X=1.7 km) shows a low degree of anisotropy (<1.5%). This zone corresponds to a low seismic velocity anomaly (Thurber et al., 2004; Hole et al., 2006; Malin et al., 2006) and high electric conductivity (Unsworth and Bedrosian, 2004), and is interpreted to be a fault-bounded wedge of late Cenozoic sedimentary rocks with extensive fracturing and saline fluids. The low degree of anisotropy in this wedge may suggest that the fractures do not have a preferential orientation but may be distributed relatively randomly. This phenomenon is evidenced from the Pilot Hole and SAFOD main hole image logs that show a lack of preferential orientation of the faults and fractures (Boness and Zoback, 2006). In this case, the anisotropy is likely to be stress induced with the fast polarization direction correlating with the direction of $S_{Hmax}$. This is supported by shear-wave splitting analysis results showing that the fast polarization direction almost perpendicular to the SAF (Fig. 1). A similar feature of low anisotropy in the sedimentary wedge is also observed in the cross-sections southeast of SAFOD. However, at shallow depths to the northwest of SAFOD (Y>0), fault zone anisotropy is relatively high (Figures 9 and 10).

Within the fault zone, strong anisotropy persists to a depth of ~4 km and most of earthquakes down to this depth fall in a zone of high anisotropy (Figures 9 and 10). At greater depths from ~4 km to ~ 8 km, the earthquakes are located inside a low anisotropy zone with K anisotropy percentage of ~1%.

## 6 TEMPORAL BEHAVIOR OF ANISOTROPY

Most of the previous studies on temporal changes of crustal anisotropy were based on an analysis of seismic data with a mixture of ray paths sampling different regions of crust (e.g. Piccinini *et al.* 2006). As shown in the previous sections, the observed SWS parameters are strongly dependent on ray paths. It is difficult to extract reliable temporal signals without carefully eliminating spatial effects. The most robust way of separating temporal changes from spatial variations is to analyze shear wave splitting using clusters of similar earthquakes (e.g. Aster *at al.* 1990; Liu *et al.* 1997; Liu *et al.* 2004; Peng & Ben-Zion 2005). In the time periods before and after the 2004 Parkfield M 6.0 earthquake, numerous microearthquakes were recorded by local temporary and permanent networks. These seismic waveforms provide a rare opportunity to investigate temporal behavior of SWS associated with a nearby M 6.0 earthquake using clusters of similar events. We identified similar events by performing waveform cross-correlation on a total of 2330 events recorded by NCSN stations using BCSEIS (Du *et al.* 2004). These events span the period January 2000 to June 2005. The time windows for the cross-correlation calculation are from 0.32 sec before the P arrival to 0.96 sec after, so that we would not rule out those potential candidates with dissimilar S waves due to a possible change of anisotropy. Many clusters of similar events with CCC values larger than 0.98 were found. The NCSN stations are mainly only vertical component, thus we instead analyzed SWS from available three-component HRSN waveforms for a number of representative clusters. Fig. 11 shows waveforms for seven clusters of similar events. The waveforms were rotated into the fast component (red) and slow component (blue) with the measured PDs, and the slow components were advanced with the obtained TDs. The vertical lines indicate the window length for SWS analysis. Similarity between the fast and slow shear waveforms within

these windows clearly shows the existence of SWS. The locations of these clusters are indicated in Fig. 1 by cluster numbers. Fig. 12 shows the observation times for each cluster, and the obtained SWS parameters from these waveforms are listed in Table 2. In order to estimate TD variations in each cluster more accurately, we employed another scheme as described in Bokelmann & Harjes (2000) and Peng & Ben-Zion (2005) and list the calculated results in Table 2 as well. We rotated the horizontal seismograms into the fast and slow components using the obtained fast PDs and aligned them by cross-correlating P phases. Then we calculated the S-P travel time variations, in relation to the first event in each cluster, for both the fast and slow components by waveform cross-correlation in a window the same as the one used in SWS analysis. The difference in the S-P travel time variation between the fast and slow components gives the TD change for the given event in each cluster. The great similarity (usually CCC > 0.99) in the fast and slow S wave shapes for these events in a given cluster guarantees a very accurate measurement of the S-P travel time variation, and therefore the TD change.

**Table 2** Measured SWS parameters from seven clusters of similar events. FDT and SDT are the S-P travel time variations relative to the first event in each cluster for the fast and slow components, respectively. VTD is the calculated TD change based on FDT and SDT.

| Cluster | Station | Event ID | DP($^o$) | +/- | TD(s) | +/- | FDT(s) | SDT(s) | VTD(s) |
|---|---|---|---|---|---|---|---|---|---|
| 1 | MMNB | 2003232210011 | 179 | 15 | 0.052 | 0.006 | - | - | - |
| 1 | MMNB | 2004266211517 | 3 | 10 | 0.053 | 0.006 | 0.0011 | 0.0000 | 0.0011 |
| 1 | VCAB | 2003232210011 | 0 | 15 | 0.109 | 0.007 | - | - | - |
| 1 | VCAB | 2004266211517 | 4 | 12 | 0.104 | 0.006 | -0.0008 | 0.0010 | -0.0018 |
| 2 | SCYB | 2002101023109 | 97 | 8 | 0.031 | 0.006 | - | - | - |
| 2 | SCYB | 2003340035731 | 98 | 12 | 0.029 | 0.007 | -0.0026 | 0.0000 | -0.0026 |
| 2 | SCYB | 2004016001220 | 98 | 8 | 0.031 | 0.006 | 0.0000 | 0.0000 | 0.0000 |
| 2 | SCYB | 2005176073742 | 98 | 12 | 0.029 | 0.006 | -0.0032 | 0.0000 | -0.0032 |
| 3 | SCYB | 2002216183823 | 90 | 10 | 0.149 | 0.009 | - | - | - |
| 3 | SCYB | 2003070191056 | 90 | 9 | 0.149 | 0.008 | 0.0027 | 0.0000 | 0.0027 |
| 3 | SCYB | 2003082161507 | 89 | 10 | 0.150 | 0.009 | -0.0016 | 0.0000 | -0.0016 |
| 3 | SCYB | 2004010031536 | 90 | 8 | 0.148 | 0.008 | 0.0000 | 0.0000 | 0.0000 |
| 3 | SCYB | 2005119194040 | 90 | 9 | 0.148 | 0.009 | 0.0000 | 0.0000 | 0.0000 |
| 4 | MMNB | 2003046092406 | 7 | 12 | 0.114 | 0.007 | - | - | - |
| 4 | MMNB | 2004275185526 | 9 | 11 | 0.114 | 0.008 | 0.0000 | 0.0000 | 0.0000 |
| 4 | SCYB | 2003046092406 | 121 | 14 | 0.077 | 0.012 | - | - | - |
| 4 | SCYB | 2004275185526 | 122 | 14 | 0.077 | 0.012 | -0.0038 | -0.0051 | 0.0013 |
| 5 | SCYB | 2003015134757 | 123 | 11 | 0.076 | 0.012 | 0.0000 | - | - |
| 5 | SCYB | 2004295051949 | 122 | 13 | 0.078 | 0.013 | -0.0014 | 0.0000 | -0.0014 |
| 5 | VCAB | 2003015134757 | 22 | 18 | 0.019 | 0.004 | - | - | - |
| 5 | VCAB | 2004295051949 | 25 | 20 | 0.018 | 0.005 | 0.0000 | 0.0008 | -0.0008 |
| 6 | MMNB | 2001234121847 | 41 | 12 | 0.096 | 0.006 | - | - | - |
| 6 | MMNB | 2002091215050 | 42 | 12 | 0.096 | 0.007 | 0.0015 | 0.0025 | -0.0010 |
| 6 | MMNB | 2002329132241 | 42 | 12 | 0.096 | 0.007 | -0.0002 | -0.0009 | 0.0007 |
| 6 | MMNB | 2003323072919 | 42 | 14 | 0.096 | 0.007 | -0.0019 | -0.0012 | -0.0007 |
| 7 | VCAB | 2004282084619 | 6 | 11 | 0.102 | 0.006 | - | - | - |
| 7 | VCAB | 2005026033557 | 5 | 12 | 0.103 | 0.006 | 0.0015 | 0.0012 | 0.0003 |
| 7 | VCAB | 2005169082558 | 0 | 12 | 0.103 | 0.005 | 0.0017 | 0.0012 | 0.0005 |

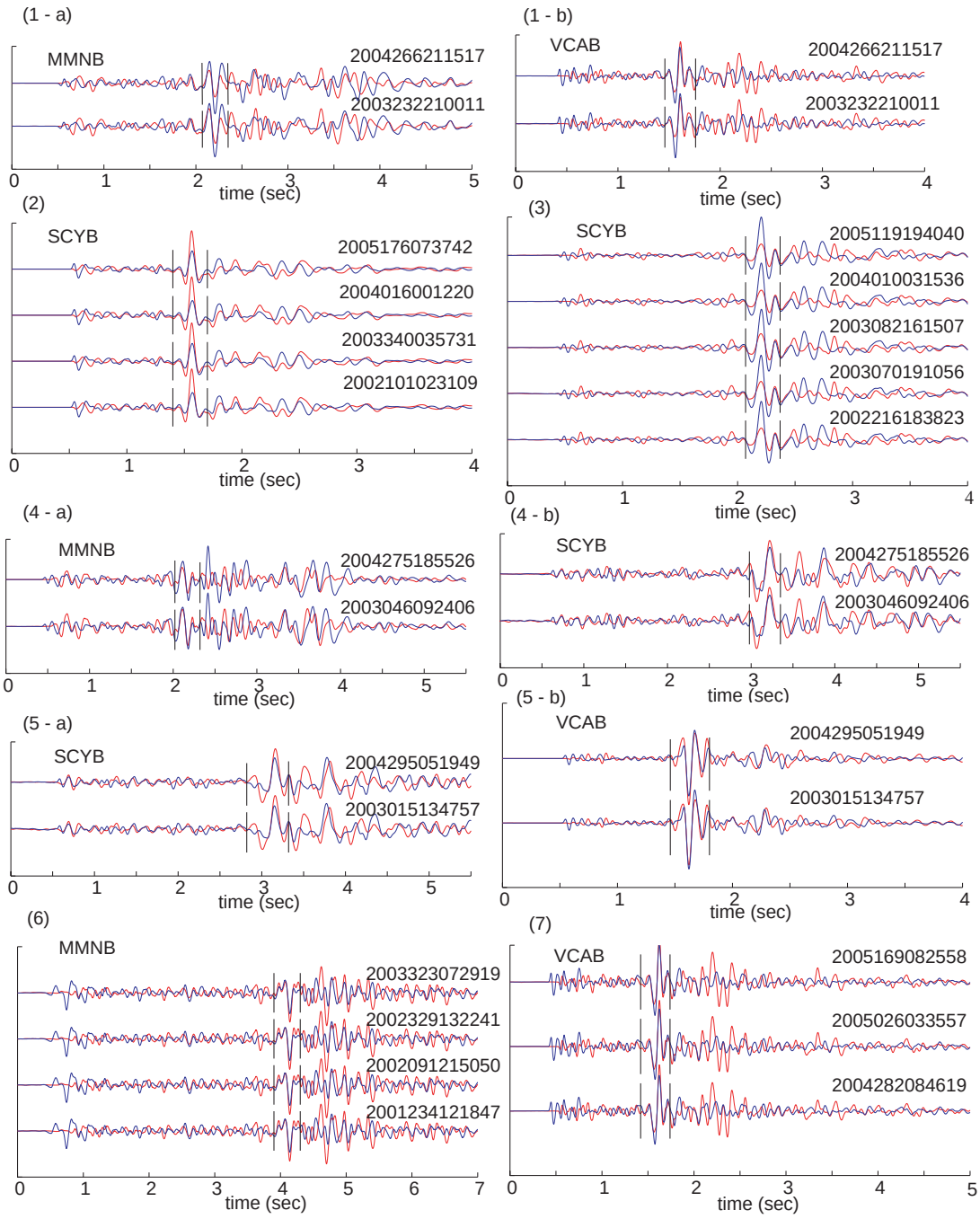


**Figure 11** Waveforms for seven clusters of similar events. The red and blue lines represent the fast and slow components, respectively. The fast components are aligned at the P arrivals and the slow shear waves are advanced with the observed TD. Vertical lines in each pair of traces indicate the time windows for SWS analysis. The number above each waveform pair gives the event information consisting of four-digit year, three-digit day in the year, two-digit hour and two-digit second of the earthquake occurrence time. Figures (1)-(7) correspond to clusters 1-7, respectively.

Clusters 1, 4, 5 and 7 are located midway between station MMNB and the town of Parkfield. This portion of the SAF ruptured in the 2004 M 6.0 Parkfield earthquake. Cluster 1 has two events spanning a ~400 day period right before the mainshock. Clusters 4 and 5 each have two events and each pair has one event right before and the other after the mainshock. Cluster 7 consists of three aftershocks. Clusters 2 and 3 are located near station SCYB and each has several events including one aftershock. Cluster 6 is located at the far northwest portion of the SAF in the study region and has four events spanning a ~1000 day period before the earthquake. From Table 2 we can see that the measured TDs from both methods for each cluster at given station vary within a few milliseconds, and the corresponding PDs are also very stable with variations much less than the measurement errors. We note that cluster 6 might be out of the SWS windows. However the observed clear SWS and stable SWS parameters for these events also give meaningful temporal signals of anisotropy. The great similarity (with CCC values for entire traces around 0.99) in waveforms indicates that events within each cluster have an almost identical location.

Thus spatial variation of anisotropy can be effectively eliminated. The temporal behavior of SWS parameters extracted from these clusters shows that there is no observable systematic temporal change in crustal anisotropy around the time of the 2004 M 6.0 earthquake. The temporal change of TDs in the same area before an M 4.0 earthquake based on analyzing similar events was reported in Liu *et al.* (1997). However, the CCC values between the "similar events" used in their study are within the range 0.51 - 0.96. The locations for events in such groups could vary significantly. Therefore their findings may not have effectively eliminated the contamination of spatial variations.

Peng & Ben-Zion (2005) found the systematic S-P travel time variations, which are appreciably larger than the measured TD variations, around the 1999 M 7.1 Düzce earthquake. However, from Table 2 we can see that the S-P travel time variations are not larger than the TD variations in our measurements. This is probably due to the fact that the borehole recordings for these HRSN stations are less affected by ground shaking caused by the main shock (e.g. Rubinstein & Beroza 2005).

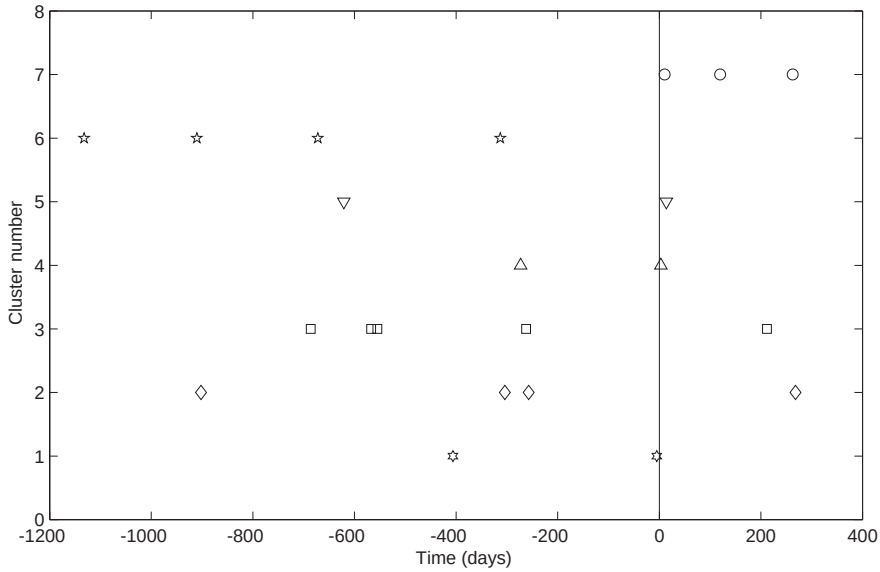


**Figure 12** Time coverage of seven clusters of similar events used in SWS analysis. The vertical line indicates the occurrence time of the September 28, 2004 Parkfield earthquake.

## 7 DISCUSSION

We systematically analyzed shear wave splitting on a waveform data set observed at 67 temporary and permanent stations in an area around the SAFOD site. Our analysis results from these densely deployed stations give a comprehensive view of the spatial distribution of anisotropy in the area surrounding the SAF zone near Parkfield. Rose diagrams show that the distributions of PDs are scattered for most of the stations. This is probably due to a strong variation of anisotropy present in the crust beneath each station at certain depth range. As a complementary way to map the lateral distribution of anisotropy from the observed SWS parameters, we also plot PDs and TDs at the positions where the ray paths intersect with a horizontal section at a certain depth. The results show clear patterns with strong lateral heterogeneity. In general, the measured PDs around the SAF zone and to the northeast are parallel or subparallel to the SAF strike, whereas some of the measurements on the southwest side of the fault are oriented NNE, which approximates the direction of local maximum horizontal compressive stress. The fault zone parallel PDs likely reflect the structural anisotropy associated with the SAF and its subsidiary faults, while the $\sigma_H$ parallel PDs probably indicate the existence of the stress-induced anisotropy in the region away from the main fault. However, in some regions, the measured PDs don't conform to this pattern. There is also a strong spatial variation of TDs in the area. It seems that due to a strong velocity gradient in the near-surface crust, the measured TDs, on average, are mainly accumulated in the top 2-3 km of the crust. However, there could be much deeper anisotropy in some areas and substantial anisotropy could extend to as deep as 7-8 km. Shear-wave anisotropy tomography results confirm the above findings.

The scatter in both the PDs and TDs is related in part to the complicated ray paths around the fault zone and spatially heterogeneously distributed anisotropy structure. We note that for stations near the fault zone ray paths often bend to the southwest side of the SAF where there is higher velocity. This means that the anisotropic structures both inside and outside the fault zone contribute to the observed SWS for stations close to the fault zone. Since almost all the events are located within the SAF zone, ray paths for stations outside the fault also sample the medium within or close to the fault zone. If structural anisotropy dominates in the fault zone whereas stress-induced anisotropy controls the area outside the fault, as suggested by Boness & Zoback (2006), the measured SWS could be affected by both types of crustal anisotropy. It is also possible that anisotropy associated with sedimentary bedding plane and aligned minerals or grains play roles in the region. Therefore, such a mixture of mechanisms for anisotropy might be responsible for the complexity of shear wave anisotropy in the region.

We have searched for possible temporal variations of shear wave splitting in relation to the occurrence of the 2004 M 6.0 Parkfield earthquake using similar events. The results from seven representative clusters with clear shear wave splitting show that the waveforms belonging to a given cluster are almost identical for the entire trace. The variation of TDs is within a few milliseconds and the change in PDs within a few degrees, much less than the measurement errors (Table 2). These clusters cover a nearly four year time period around the 2004 Parkfield M 6.0 earthquake and the measured SWS parameters sample the crust close to the rupture area of the earthquake. The results show that there are no appreciable precursory, coseismic or postseismic temporal changes in SWS. A lack of temporal changes of SWS around faults is not surprising if the associated

anisotropy is due to alignment of structural fabrics, because such aligned features should be insensitive to changes of stress field. It is also possible that the change in the stress field related to the mainshock has no measurable impact on stress-induced anisotropy associated with preferential closure of vertical cracks.

## ACKNOWLEDGMENTS

Research supported by the U.S. Geological Survey (USGS), Department of the Interior, under USGS award number 06HQGR0105. The views and conclusions contained in this document are those of the authors and should not be interpreted as necessarily representing the official policies, either expressed or implied, of the U.S. Government. We are grateful for the contribution of Lee Powell and others in the PASO deployment. The instruments used in the field program were provided by the PASSCAL facility of the IRIS through the PASSCAL Instruments Center at New Mexico Tech Data Management Center. The PASO data are available through the IRIS Data Management Center. HRSN and NCSN data are provided by the Northern California Earthquake Data Center. We also thank Felix Waldhauser for sharing the NCSN dataset he assembled.

## REFERENCES

Aster, R.C., Shearer, P.M. & Berger, J., 1990. Quantitative measurements of shear wave polarizations at the Anza seismic network, southern California: implications for shear wave splitting and earthquake prediction, *J. Geophys. Res.,* **95,** 12 449-12 473.

Aster, R.C., Shearer, P.M. & Berger, J., 1991. Comments on 'Quantitative measurements of shear-wave polarization at the Anza seismic network, Southern California: implications for shear-wave splitting and earthquake prediction' by Aster, R.C., Shearer, P.M. & Berger J.—Reply, *J. Geophys. Res.,* **96,** 6415-6419.

Bokelmann, G.H.R. & Harjes, H.P., 2000. Evidence for temporal variation of seismic velocity within the upper continental crust, *J. Geophys. Res.,* **105,** 23 879-23 894.

Boness, N. & Zoback, M, 2004. Stress-induced seismic velocity anisotropy and physical properties in the SAFOD Pilot Hole in Parkfield, CA, *Geophy. Res. Lett.,* **31** L15L17.

Boness, N. & Zoback, M., 2006. A multiscale study of the mechanism controlling shear velocity anisotropy in the San Andreas Fault Observatory at Depth, *Geophysics,* **71**, NO. 5, F131-F146.

Bouin, M.-P., Tellez, J. & Bernard, P., 1996, Seismic anisotropy around the Gulf of Corinth, Greece, deduced from three-component seismograms of local earthquakes and its relationship with crustal strain, *J. Geophys. Res.,* **101,** 5797-5811.

Cochran, E., Li, Y.-G., & Vidale, J., 2006. Anisotropy in the shallow crust observed around the San Andreas Fault before and after the 2004 M 6.0 Parkfield earthquake, *Bull. Seism. Soc. Am.*, **96**, S364-S375.

Cochran, E., Vidale, J. & Li, Y.-G., 2003. Near-fault anisotropy following the Hector Mine earthquake, *J. Geophys. Res.,* **10**, 2436.

Crampin, S., 1987. The geological and industrial implication of extensive-dilatancy anisotropy , *Nature*, **328**, 491-496.

Crampin, S., Booth, D.C., Evans, R., Peacock, S. & Fletcher, J.B., 1990. Change in shear wave splitting at Anza near the time of the North Palm Springs earthquake, *J. Geophys. Res.,* **95,** 11 197-11 212.

Crampin, S. & Chastin, S., 2003. A review of shear wave splitting in the crack-critical crust, *Geophys J. Int*., **155**, 221-240.

Currie, C.A., J.F. Cassidy, R.D. Hyndman, M.G. Bostock, 2004, Shear wave anisotropy beneath the Cascadia subduction zone and western North American craton, *Geophys. J. Int.*, **157 (1)**, 341–353, doi:10.1111/j.1365-246X.2004.02175.x.

Du, W.-X, Thurber, C.H., & Eberhart-Phillips, D., 2004. Earthquake relocation using cross-correlation time delay estimates verified with bispectrum method, *Bull. Seism. Soc. Am*, **94**, pp. 856-866.

Eberhart-Phillips, D., and C.M. Henderson, 2004, Including anisotropy in 3-D velocity inversion and application to Marlborough, New Zealand, *Geophys. J. Int.*, **156**, 237-254, doi:10.1046/j.1365-246X.2003.02044.x.

Fukao, Y. 1984. Evidence from core-reflected shear waves anisotropy in the earth mantle, *Nature*, **309**, 695-698.

Hickman, S. & Zoback M., 2004. Stress orientations and magnitudes in the SAFOD pilot hole, *Geophy. Res. Lett*., **31.** L15L12.

Holmes, G.M., S. Crampin, and R.P. Young, 2000, Seismic anisotropy in granite at the Underground Research Laboratory, Manitoba, *Geophys. Prospect.*, **48 (3)**, 415–435. doi:10.1046/j.1365-2478.2000.00195.x.

Ishise, M., and H. Oda, 2005, Three-dimensional structure of P-wave anisotropy beneath the Tohoku district, northeast Japan, *J. Geophys. Res.,* **110**, B07304, doi:10.1029/2004JB003599.

Kern, H. & Wenk, H.-R., 1990. Fabric-related velocity anisotropy and shear wave splitting in rocks from the Santa Rosa Mylonite Zone, California, *J. Geophys. Res*., **95**, 11,213-11,224.

Kern, H., B. Liu, and Popp, T., 1997, Relationship between anisotropy of P and S wave velocities and anisotropy of attenuation in serpentinite and amphibolite, *J. Geophys. Res.*, **102**, 3051–3065.

Kreyszig, E., 1970. Introductory mathematical statistics, principle and methods, pp. 470 John Wiley and Sons, New York.

Leary, P.C. Crampin, S. and McEvilly, T., 1990. Seismic Fracture Anisotropy in the Earth's Crust: An Overview. *J. Geophys. Res,* **95**, 11,105-11,114.

Liu, Y., Crampin, S. & Main, I., 1997. Shear-wave anisotropy: spatial and temporal variations in time delays at Parkfield, central California, *Geophys. J. Int*., **130**, 771-785.

Liu, Y., Teng, T.-L. & Ben Zion, Y., 2004. Systematic analysis of shear-wave splitting in the aftershock zone of the 1999 Chi-Chi, Taiwan, earthquake: shallow crustal anisotropy and lack of precursory variations, *Bull. Seism. Soc. Am.*, **94**, 2330-2347.

Liu, Y., Ben-Zion, Y. & Teng, T.-L., 2005. Reply to Comment of Crampin and Gao on 'Systematic analysis of shear-wave splitting in the aftershock zone of the 1999 Chi-Chi, Taiwan, earthquake: shallow crustal anisotropy and lack of precursory variations', *Bull. Seism. Soc. Am.,* **95,** 361-366.

Liu, Y., Teng, T.-L. & Ben Zion, Y., 2005. Near-surface seismic anisotropy, attenuation and dispersion in the aftershock region of the 1999 Chi-Chi earthquake, *Geophys. J. Int*. **160**, 695-706.

McPhee, D.K., R.C. Jachens, and C.M. Wentworth, 2004, Crustal structure across the San Andreas Fault at the SAFOD site from potential field and geological studies, *Geophys. Res. Lett.*, 31, L12S03, doi:10.1029/2003GL019363.

Mardia, K.V. & Jupp, P.E., 2000. Directional Stastics, pp. 429, John Wiley, Hoboken, N.J.

Mizuno, T., Ito, H., Kuwahara, Y., Imanishi, K. & Takeda, T., 2005. Spatial variation of shear-wave splitting across an active fault and its implication for stress accumulation mechanism of inland earthquakes: The Atotsugawa fault case, *Geophys. Res. Lett.*, **32**, L20305.

Munson, C.G., Thurber, C.H., Li, Y. & Okubo, P.G., 1995. Crustal shear wave anisotropy in southern Hawaii: spatial and temporal analysis, *J. Geophys. Res.,* **100**, 20 367-20 377.

Mueller, M.C., 1991. Prediction of lateral variability in fracture intensity using multicomponent shear-wave seismic as precursor to horizontal drilling, *Geophys. J. Int.*, **107**, 409-415.

Nuttli, O., 1961. The effect of earth's surface on the S-wave particle motion, *Bull. Seism. Soc. Am.* **51**, 237-246.

Peng, Z. & Ben-Zion, Y., 2004. Systematic analysis of crustal anisotropy along the Karadere-Duzce branch of the North Anatolian fault, *Geophys. J. Int*. **159**, 253-272.

Peng, Z. & Ben-Zion, Y., 2005. Spatiotemporal variations of crustal anisotropy from similar events in aftershocks of the 1999 M7.4 Izmit and M7.1 Düzce, Turkey, earthquake sequences, *Geophys. J. Int.*, **160**, 1027-1043.

Piccinini D., Margheriti, L., Chiaraluce, L. & Cocco, M., 2006. Space and time variations of crustal anisotropy during the 1997 Umbria-Marche, central Italy, seismic sequence *Geophys. J. Int*. **167**, 1482-1490.

Rau, R.-J., Liang, W.-Z., Kao, H. & Huang, B.-S., 2000. Shear wave anisotropy beneath the Taiwan orogen, *Earth Planet. Sci. Le.*, **177**, 177-192.

Rubinstein, J. L., and Beroza, G.C., 2005, Depth constraints on nonlinear strong ground motion from the 2004 Parkfield earthquake, *Geophys. Res. Lett.*, *32*, L14313.

Saiga, A., Hiramatsu, Y., Ooida, T. & Yamaoka, K., 2003. Spatial variation in the crustal anisotropy and its temporal variation associated with a moderate-sized earthquake in the Tokai region, central Japan, *Geophys. J. Int.,* **154,** 695-705.

Shih, X.R., Meyer,R.P. & Schneider, J.F., 1989. An automated and analytical method to determine shear wave splitting, *Tectonophysics,* **165**, 271-278.

Silver, P.G. & Chan, W.W., 1991. Shear wave splitting and subcontinental mantle deformation, *J. Geophys. Res.,* **96**, 16 429-16 454.

Tadokoro, K., M. Ando, and Y. Umeda, 1999, S wave splitting in the aftershock region of the 1995 Hyogo-ken Nanbu earthquake, *J. Geophys. Res.*, **104**, 981-991.

Thayer, M.R. & Arrowsmith, J R., 2005, Fault Zone Structure of Middle Mountain, Central California, *Eos Trans.* AGU, **86**, Fall Meet. Suppl., Abstract T21A-0458.

Thurber, C., Roecker, S., Zhang, H., Baher, S. & Ellsworth, W.L., 2004. Fine-scale structure of the San Andreas fault zone and location of the SAFOD target earthquakes, *Geophys. Res. Lett*., **31**, L12S02.

Thurber, C., Zhang, H., Waldhauser, F. Hardebeck, J. Michael, A. and Eberhard-Phillips, 2006. Three-dimensional compressional wavespeed model, earthquake relocations, and focal mechanisms for the Parkfield. California, regions, *Bull. Seism. Soc. Am.*, **96**, S38-S49.

Townend, J. & Zoback, M., 2004. Regional tectonic stress near the San Andreas fault in central and southern California, *Geophys. Res. Lett.*, **31**, L15S12.

Unsworth, M., and P. A. Bedrosian, 2004, Electrical resistivity structure at the SAFOD site from magnetotelluric exploration, *Geophys. Res. Lett.*, **31**, L12S05, doi:10.1029/2003GL019405.

Zhang, Z. & Schwartz, S.Y., 1994. Seismic anisotropy in the shallow crust of the Loma Prieta segment of the San Andreas fault system, *J. Geophys. Res.*, **99**, 9651-9661.

## Bibliography

Liu, Y., **H. Zhang**, C. Thurber, S. Roecker (2007), Shear wave anisotropy in the crust around the San Andreas fault near Parkfield: spatial and temporal analysis, submitted to *Geophys. J. Int.*